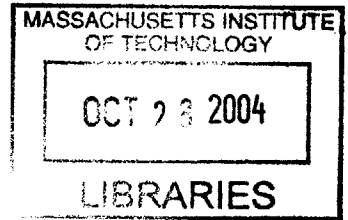# Design of a Wideband, 100 W, 140 GHz Gyroklystron Amplifier

by

Colin D. Joye

B.S., Electrical Engineering and Computer Science (2002)
Villanova University

Submitted to the Department of Electrical Engineering and Computer
Science
in partial fulfillment of the requirements for the degree of

Master of Science in Electrical Engineering

at the

MASSACHUSETTS INSTITUTE OF TECHNOLOGY

September 2004

Author . . . .
Department of Electrical Engineering and Computer Science
ıgust 6, 2004

Certified by . . . .
Richard J. Temkin
Senior Research Scientist, Deptartment of Physics
Supervisor

Accepted by . . . .
Arthur C. Smith
Chairman, Committee on Graduate Students
Department of Electrical Engineering and Computer Science

Design of a Wideband, 100 W, 140 GHz Gyroklystron Amplifier

by

Colin D. Joye

B.S., Electrical Engineering and Computer Science (2002)

Villanova University

Submitted to the Department of Electrical Engineering and Computer Science
on August 6, 2004, in partial fulfillment of the
requirements for the degree of
Master of Science in Electrical Engineering

Abstract

The design study of a 140 GHz, 100 W continuous wave gyroklystron amplifier is presented. The device is intended for use in Dynamic Nuclear Polarization (DNP) enhanced Nuclear Magnetic Resonance (NMR) spectroscopy experiments. The gyroklystron has five cavities and operates in the TE(0,2) mode with a low power electron beam. The design was performed using MAGY, a nonlinear code for modelling gyrotron devices. The design process of the gyroklystron starting from the linear theory to the optimization of the final design in MAGY has been described in detail. Stagger tuning was employed to broadband the device. The design yields 130 W peak power, 36 dB saturated gain, and a -3 dB bandwidth of over 1 GHz (0.75%) with a 15 kV, 150 mA electron beam having a beam pitch factor of 1.5, radius of 0.64 mm and calculated perpendicular momentum spread of 4%. Preliminary designs of the Magnetron Inject Gun (MIG), the input and output couplers, and the mode converter to transform the TE(0,2) operating mode to the HE(1,1) mode for low loss transmission of the output power are also presented. The design meets the specifications for the DNP experiment.

Thesis Supervisor: Richard J. Temkin
Title: Senior Research Scientist, Deptartment of Physics

Acknowledgments

First of all, I am most grateful to my Lord and Savior, Jesus Christ, without whom all of my labor is without meaning. Throughout all of my difficult days in undergrad, many of which started with a 5:30 AM paper route, and all of my stressful days at MIT, many of which started before 5:00 AM with prayer, God was the only one I could turn to for my daily strength. My whole existence belongs to God and for His grace and mercy, I am eternally thankful.

Secondly, I'd like to thank my parents, Dr. Donald Joye and Claudia Joye, who educated my brothers (Gavin and Chris) and I for twelve years each at home so that we could learn the values and virtues not taught in the schools. They sacrificed much of their time and comfort to help us and several hundred other homeschooling families bring their children up in the way they thought was best. I am especially thankful to my father, whose laboring many years as a professor at Villanova University allowed me to get a high quality education for free. I thank my mom for her encouragement, help with all planning and administrative things and especially for food! My brothers have been a source of encouragement and good times as we grow together.

Wherever I went, I was blessed with a multitude of friends who have kept me thinking about what's really important in life - People. A year's worth of research cannot outweigh the joy of deepening friendships. Over the years, I have been involved in dozens of activities: Years of hard training in Tang Soo Do taught by my instructor, Master David Kremin, have taught me the importance of discipline and tenacity, as well as how to teach others; my interests in music, audio, electronics, and art have led me to many places I never dreamed of; my interest in languages led me to learn Korean and meet many wonderful Korean friends at First Korean Church in Cambridge, including my (hopefully) future wife, Heidi.

From my lab, I'd like to thank my advisor, Dr. Rick Temkin, who works harder than all of us, Dr. Michael Shapiro for his help on mode converters and codes, Dr. Jagadishwar Sirigiri for his never-ending help in everything, and Eunmi Choi, who shared in many helpful and encouraging conversations in our office.

Contents

List of Figures

13

List of Tables

Chapter 1

Introduction

The gyroklystron amplifier is a high frequency vacuum electron device (VED) used to amplify electromagnetic waves with wavelengths on the millimeter scale to higher power levels. The gyroklystron is part of a larger class of general fast wave gyro-devices that utilize the electron cyclotron resonance maser (CRM) instability. The possibility of an electron beam interacting with an electromagnetic wave was known by the end of the 1950s, laying the foundation for all gyro-devices [1]. In particular, the gyrotron oscillator research that has been going on since the 1970s has focused primarily on applications for plasma heating in the millimeter band range of 28 GHz to 170 GHz, at power levels typically greater than hundreds of kilowatts or more [2]. More recently, gyrotron amplifier research has begun to take root in fertile fields such as radar [3], target tracking, imaging, cloud physics [4] [5] and experiments utilizing Dynamic Nuclear Polarization (DNP) [6] [7].

In gyro-devices, a weakly relativistic electron beam gives up energy to radio frequency (RF) electromagnetic fields in the cavities through bremsstrahlung, a process whereby the electrons emit radiation as they experience forces from the electromagnetic fields. The term *fast wave* comes about because the phase velocity of the electromagnetic wave in the interaction structure is faster than the speed of light. In this regime, the cavity structures are typically several wavelengths long and the energy is extracted from the perpendicular component of the electron momentum. In contrast, the interaction structure of the slow wave device keeps the RF phase veloc-

ity below the speed of light so that the electrons travel in synchronism with the RF fields. When this happens, Cherenkov radiation is emitted by interaction with the parallel component of the electron's velocity instead of the perpendicular component. In both slow wave and fast wave devices, the transverse dimensions of the interaction structure scale inversely with frequency, which limits the power that can be safely generated in the structure due to the increased ohmic losses. Fast wave devices can, however, operate in higher order modes very efficiently. This allows the dimensions of the interaction structures to be larger, making it possible to generate higher power while limiting the thermal losses in the structure. The efficiency of slow wave devices is very poor at higher order modes and thus the fast wave devices have a distinct edge at the millimeter wave frequencies and above.

The gyroklystron amplifies RF via a focused electron beam travelling through a series of resonant cavities. It is the fast wave extension of the klystron, which is itself a slow wave device used for generating microwaves. Gyroklystrons are known for their high efficiency and ability to provide high power in a frequency band that is out of reach for both slow wave and laser devices (Fig. 1-1) [8]. Among the competitors for the microwave band are conventional microwave tubes such as klystrons, magnetrons, travelling wave tubes (TWTs), backward-wave oscillators (BWOs) and other slow-wave devices. In the millimeter band, the competition thins out, leaving gyro-devices as the only practical high-power sources. BWOs, Orotrons, and even some solid state devices are capable of producing power in the millimeter bands, but do not extend to sub-millimeter wavelengths at the necessary power levels. By operating at integer harmonics of the fundamental, gyrotron devices have achieved operation frequencies of up to 889 GHz [9].

1.1 Motivations for the Gyroklystron

Since this gyroklystron will be incorporated into an existing DNP experiment at the Francis Bitter Magnet Laboratory, Cambridge Massachusetts, it is a desirable feature that the source be capable of continuous wave (CW) operation as well as nanosecond-
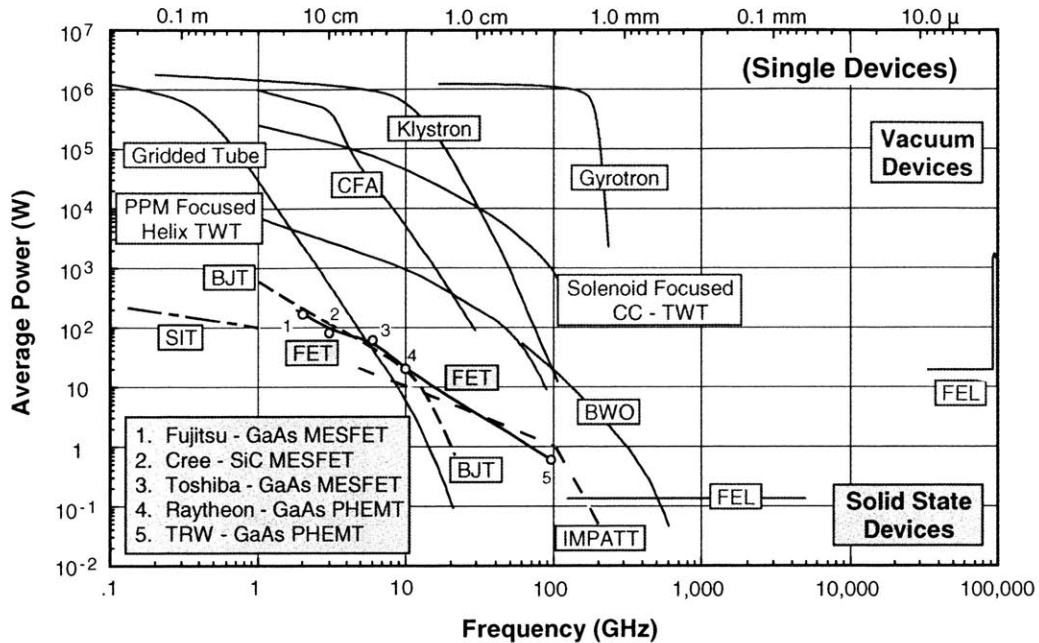
Figure 1-1: Recent advances in vacuum electron device technology showing gyro-devices pushing the frontier to higher power and higher frequency.

scale short pulses. The short-pulse capability requires a fairly wide bandwidth and a high amount of phase stability. The CW operation is much easier to achieve at low electron beam power, whereas an amplifier would lend itself to phase-stable short pulses [10]. Furthermore, lab safety is an important consideration, as higher voltage makes shielding the power wires considerably more challenging. Unfortunately, the lowering of beam voltage in most amplifier devices causes the bandwidth to become narrow, but the gyroklystron provides a series of cavities that can be tuned to different resonant frequencies to widen the bandwidth at the expense of amplifier gain, a method known as stagger tuning [11]. The cluster cavity [12] technique can theoretically widen the bandwidth without losing gain if the cavities are uncoupled, but this has yet to be achieved in practice. Another challenge of low beam power is that the gain is severely restricted at low beam currents.

19

1.2 Description of Operation

In all gyro-devices, an electron beam is emitted from an indirectly heated cathode and guided along a precision magnetic field through a single cavity, series of cavities, or a long gyro-travelling wave tube (gyro-TWT) section. The electron beam consists of many electrons gyrating around the magnetic field lines in a small helix with a cyclotron frequency near the operating frequency of the device as they propagate from the cathode side of the tube to the collector side. These small helicies form a larger hollow annular ring beam.

If the Larmor orbits of the electrons are smaller than the guiding center radius (average radius of the hollow annulus), then the device is called a small orbit device. On the other hand, if the Larmor radius is greater than or equal to the guiding center radius, the device is said to be a large orbit device. A small orbit beam can be easily generated by a Magnetron Injection Gun (MIG), and this is the type of beam we will utilize here. The generation of a large orbit beam is more complicated and is usually achieved by imparting a kick to a linear beam by either a magnetic cusp or a microwave kicker.

Energy is extracted in the gyrotron interaction by the relativistic cyclotron resonance maser instability in which the electrons are phase bunched in the azimuthal direction due the RF fields. The bunches grow along the beam, and if the operating frequency is slightly higher than the cyclotron frequency of the electrons, the bunches end up in the decelerating phase of the microwave field and give up it energy to it [13]. Only the transverse energy is extracted from the electron beam during a CRM fast wave interaction and hence an electron beam with significant transverse energy is chosen in a gyrotron device. Typically the *pitch factor*, or the ratio of the transverse energy to the longitudinal energy of a gyrotron beam varies from 0.5 to 2.0 and is given the symbol α.

At the end of the interaction, the beam has lost a significant amount of its original energy to the RF fields in the cavities and is collected by a thermally cooled collector. The remaining RF fields are extracted from the tube and sent through waveguides to
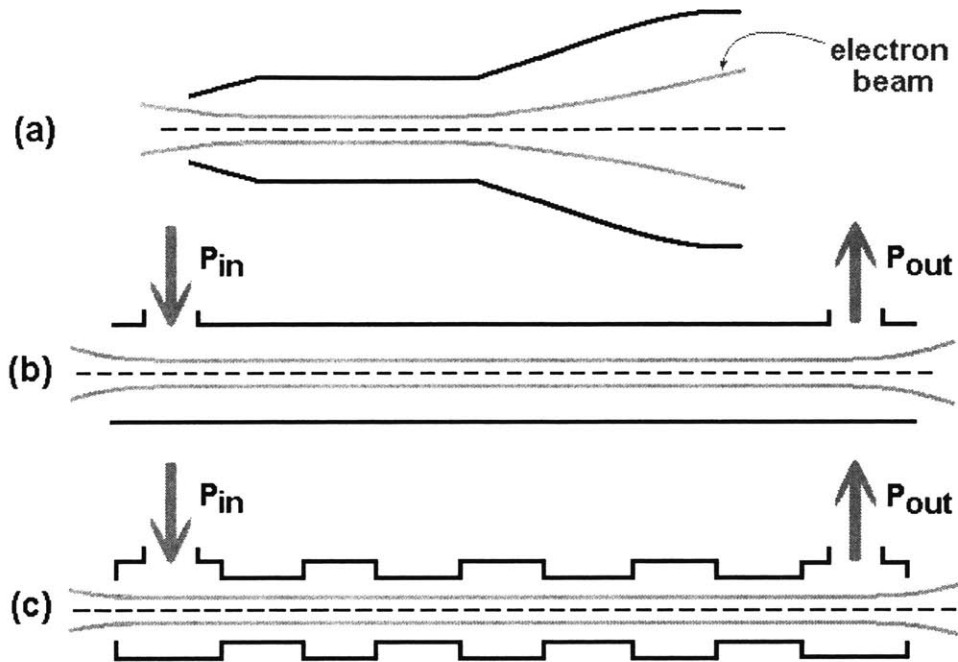
Figure 1-2: Common gyro-device cavity profiles with an electron beam: (a) gyrotron oscillator; (b) gyro-TWT; (c) gyroklystron.

the desired application. The particular variation of the interaction circuit falls into several categories [14]:

1.2.1 Gyrotron

The gyrotron oscillator consists of a short cylindrical resonant cavity section bounded on either side by a down-taper and up-taper (Fig. 1-2a). The energy is extracted from the uptaper section and often sent through an internal quasi-optical mode converter in high power gyrotrons. High power gyrotrons usually operate in a high order mode, such as the $TE_{22,6}$ mode so that a larger electron beam diameter can be used to reduce the problem of space charge [15]. A mode converter is necessary to change this mode to a Gaussian-like mode to further reduce spurious mode conversion and transmission loss through a waveguide transmission line.

1.2.2 Gyro-TWT

Gyro-TWTs are capable of very high gain and large bandwidth due to a near matching of the waveguide mode and cyclotron mode and because the group velocity is very close to the electron beam velocity. The interaction structure is most simply a waveguide with no resonant structures, so the bandwidth can be quite large (Fig. 1-2b). Velocity spread is typically the limiting factor for how long a structure can be. The gyro-TWT often suffers from problems with instabilities and self-oscillation due to spurious backward waves, although the more recent use of heavily-loaded, lossy TWT waveguides was found to be a good way of controlling these problems. Gyro-TWTs have not been built at very low beam voltages.

Another version of the gyro-TWT uses confocal waveguide to avoid the use of expensive, fragile and often temperature-sensitive lossy ceramic materials. The confocal gyro-TWT was first successfully demonstrated at MIT [16]. The large gap on either side of the waveguide lowers the total Q by diffraction, allowing it to be easily built without the use of lossy ceramics. In a confocal waveguide, the diffractive losses from the open sidewalls allow the suppression of lower-order modes. Thus, using it in a gyro-TWT allows operation in higher-order modes without mode competition. This in turn allows the the use of an interaction structure with larger transverse dimensions and hence higher power handling capability. Because part of the annular electron beam sees no RF fields, efficiency is lower than the gyro-TWT. Mode conversion may also be more difficult from the hybrid modes to lower-order Gaussian beams.

The new possibility exists of building a gyro-TWT using Photonic Band Gap (PBG) structures. The PBG gyro-TWT would consist of a 2-D lattice of rods periodically spaced with a defect in the lattice where some rods are removed. The PBG interaction structure can be designed so that the backward wave frequency lies in the passband of the PBG structure and hence leaks out of the lattice. This is likely to dramatically reduce the Q of the structure for the backward wave mode and allow operation at higher beam currents in the forward wave amplifying mode. Hence

the result is a mode-selective structure supporting only the design mode. A PBG gyrotron oscillator was demonstrated at MIT [17]. A PBG amplifier has yet to be built.

1.2.3 Gyroklystron

A gyroklystron consists of a series of nearly isolated prebuncher cavities, each of which bunches the electrons such that gain occurs in each cavity (Fig. 1-2c). In theory, the gyroklystron can have as much as 18 dB of power gain per cavity in the linear regime [18], lending gyroklystron devices to relatively short circuits. A small RF signal is coupled into the first cavity, then amplified in each cavity and finally extracted at the end. Gyroklystrons typically have very good linearity, less sensitivity to velocity spread and can have considerably wide bandwidth even at low beam voltages. Since the gyroklystron typically has a more narrow bandwidth than the gyro-TWT, it is also less noisy. This device, however, is more difficult to build, since several cavities have to be tuned properly and the alignment of the cavities with the electron beam can be difficult. Furthermore, the drift spaces, where ideally no fields exist, are susceptible to a plethora of modes and resonances in practice.

A common method for adjusting the Q factor of each cavity in the gyroklystron is to use lossy ceramics. However, other possibilities exist, such as lossy tunable slots in the cavity that would lower the Q by diffracting some power out. Large slots could be used in the drift sections to allow the fields to leak out and be absorbed by larger lossy ceramics.

1.2.4 Gyrotwystron

A gyrotwystron is a hybrid device consisting of a gyroklystron section followed by a gyro-TWT section. Utilizing this configuration rather than a plain gyroklystron alone, higher bandwidth can be achieved, as well as extra protection against RF breakdown. Another version is the inverted gyrotwystron, where the travelling wave section appears first. The gyrotwystron is typically more susceptible to oscillations

Table 1.1: Gyroklystron Achievements

Source	V_0 [kv]	I_0 [A]	P_{out} [kW]	eff	f_0 [GHz]	BW [MHz]	$gain$ [dB]
CPI, NRL [19]	55	6.0	10.2 (ave)	31%	95	700 (0.74%)	33
NRL [20]	72	9.6	208 (pk)	30%	35	178 (0.51%)	53
CPI, NRL [21]	53.7	5.1	72 (pk)	27%	95	410 (0.43%)	50
CPI, NRL [21]	56	4.4	84 (pk)	33.8%	95	370 (0.39%)	40
CPI, NRL [22]	58	4.2	60 (pk)	25%	93	640 (0.68%)	27
CPI, NRL [23]	65	6	80 (pk)	29.5%	94	600 (0.64%)	24.7
Nusinovich [24]	40	0.3	1.0 (pk)	8.5%	360	72 (0.02%)	
Proposed GKL at MIT	15	0.15	0.10 (cw)	5%	140	1000 (0.71%)	36

than the gyroklystron. Not many have been built and the documentation is rather sparse.

1.2.5 Gyro-BWO

In a BWO, the output frequency is directly adjusted by the operation voltage, but higher magnetic fields are required for the BWO than for other gyro-devices because of a negative Doppler shift, making the BWO undesirable at very high frequencies. BWOs also suffer from a relatively low efficiency and low output power.

1.3 Previous Gyroklystron Work

Many advances have been made recently in the field of gyroklystron research. Tab. 1.1 lists several examples of gyroklystrons that have been built recently.

Some gyroklystron design advances and variations include a dual-cavity coaxial gyroklystron [25], third-harmonic gyroklystrons [26], and sub-millimeter second-harmonic designs [24]. In addition, many advances have been made in the theory of gyroklystrons, such as the optimization of gyroklystron efficiency [18], AC space charge analysis [27], the effects of penultimate cavity position and tuning [28], and the theory of stagger tuning [29].

24

1.3.1 Novel Features of this Design

Because it is desirable to have CW operation on the order 100 W, a low beam power is necessary to maintain reasonable efficiency. A low beam voltage would lend itself to lab safety. Thus one aspect of this design that is considered novel is low beam power. Operation as such low voltage (leading to a more weakly relativistic beam) and low current poses significant challenges. Low voltage causes the bandwidth to become more narrow as the cyclotron resonance line intersects the waveguide modes near cutoff and also makes it difficult to avoid problems with space charge. Low current significantly reduces the gain. Most gyroklystron designs have operated in the neighborhood of 60 kV and above 4 A, whereas this design focuses on 15 kV at 0.15 A. No gyroklystron has ever been designed with such a low beam current.

The use of Photonic bandgap (PBG) resonators has been evaluated to reduce or eliminate mode competition in the cavity circuit as well as a novel method for adjusting the Q in the cavity without use of lossy dielectrics or ceramics.

1.4 Thesis Outline

Chapter two is an overview of the whole design, chapter three summarizes the theory behind the operation of gyroklystrons, chapter four focuses on the cavity circuit, chapter five shows the details of the electron gun design, chapter six touches on the nonlinear uptaper and mode converter and chapter seven is the conclusion.

Chapter 2

Overview of Program

Here is presented an overview of the whole test bed already in place at the Francis
Bitter Magnet Lab (FBML) in Cambridge, MA, as well as an overview of the proposed
gyroklystron amplifier.

2.1 Overview of the Current Experimental Setup

The current Dynamic Nuclear Polarization enhanced Nuclear Magnetic Resonance
(DNP/NMR) test bed at the FBML consists of a 140 GHz gyrotron, waveguides, a
DNP probe and another superconducting magnet (Fig. 2-1). The gyrotron delivers
approximately 15 Watts in the TE_{01} mode into a snake mode converter which trans-
forms it to the TE_{11} mode before it propagates down straight copper pipes. Two
90° miter bends exist before the oversized waveguide is tapered down to fundamental
waveguide. The total losses were measured previously to be approximately 6.4 dB
with theoretical losses totalling 3.7dB [30]. At the probe, approximately 1 to 2 watts
of power is delivered into the sample.

In this DNP test bed, the 140 GHz gyrotron will be replaced with the proposed
140 GHz amplifier. The amplifier will deliver approximately 100 Watts in the TE_{01}
mode into the existing snake converter. If the existing waveguide is also used, the
resulting power at the probe is expected to be in the tens of Watts. A newer sys-
tem including a TE_{11} to HE_{11} scalar horn mode converter and low-loss corrugated
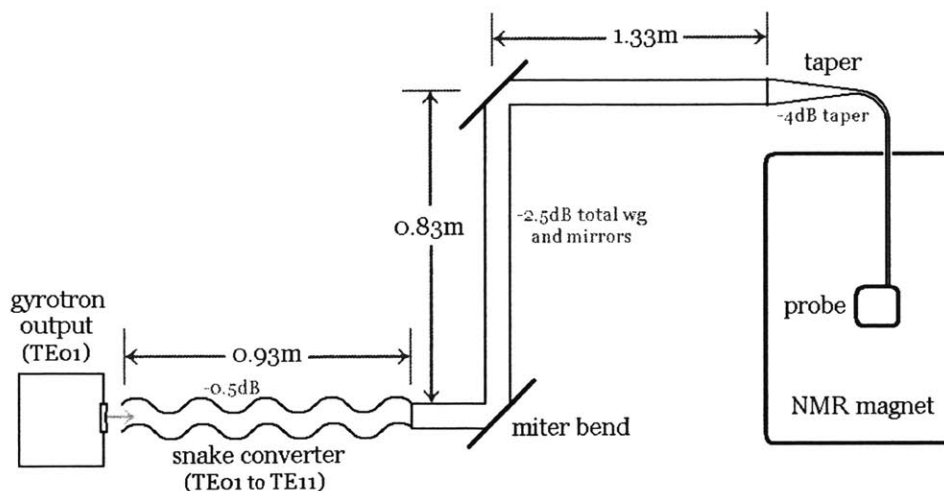
Figure 2-1: The current DNP test bed utilizes a 140 GHz gyrotron, waveguide with 2 miter bends and a downtaper, a DNP probe, and another superconducting magnet. Losses were measured previously.

waveguide lines are also available to lower the spurious mode conversion and waveguide losses, if needed. The amplifier will feature ease of frequency tunability where previously only a single frequency was used, and it will also allow nanosecond-scale short pulses to be sent to the samples.

2.2 Overview of the Gyroklystron Operation

Referring to the block diagram of the gyroklystron in Fig. 2-2, an indirectly heated cathode ring in the electron gun at one extreme of the gyroklystron tube emits an annular beam of electrons by thermionic emission in a carefully designed region with high electric fields. The electrons adiabatically spiral around the magnetic field lines created by the magnet. The size of this spiral is determined by the Larmor radius which is related to the static magnetic field and the relativistic mass of the electrons. The electrons are initially randomly distributed in phase over the range $(0, 2\pi)$ and are assumed to produce a uniform current density over the area of the annular ring.

The gyroklystron cavity circuit consists of an alternating series of cavities and drift spaces. In the first cavity, RF power is coupled in from an external source. As

28
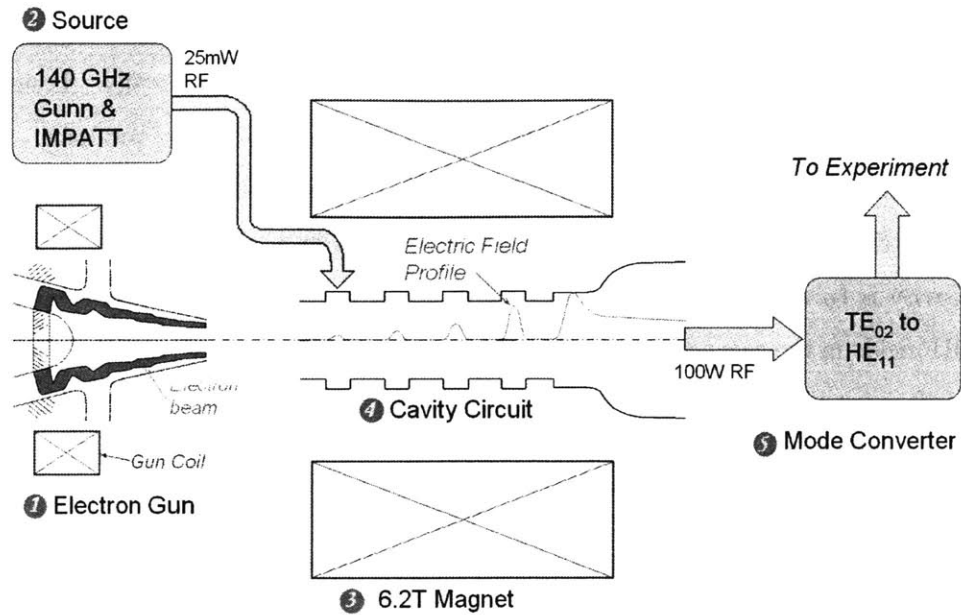
Figure 2-2: The system block diagram: (1) Electron gun (MIG), (2) Solid state RF source, (3) Superconducting magnet, (4) Cavity circuit (gyroklystron shown) and (5) Mode converter.

the electron beam enters the first cavity, the electric field produces a force on the electrons as they spiral around the magnetic field lines. This force not only changes the phase of the electrons as their orbits are slowed down and sped up, but it also causes the electrons to emit bremsstrahlung radiation, which is superimposed over the existing fields in the cavity. This effect of changing the perpendicular momentum of the electrons by interaction with an electric field leads to a process called bunching, which causes a majority of the electrons to emit bremsstrahlung in phase coherently.

After the first cavity, the electron beam enters a cutoff region called the drift space where the electromagnetic fields cannot propagate (evanescence). The electron phases, being affected by the RF-induced forces in the first cavity, continue to evolve in the drift space in a process known as ballistic bunching. The purpose of the drift space is two-fold: To isolate adjacent cavities from coupling to one another, and to allow the bunching to evolve. A beam that is more highly bunched tends to emit bremsstrahlung in phase and hence emits more RF energy. However, if the beam

29

is allowed to evolve too long, or if the bunching process is forced too strongly, an overbunching may result in which the efficiency drops dramatically. Longer drift spaces then have the effect of increasing the gain, unless they are too long.

Upon entering the second cavity, where no pre-existing RF is present, the electrons give off RF at the Doppler-shifted frequency given by the beam line relation. If the cavity is tuned properly, the bunching in the beam will be reinforced and the total RF fields in the second cavity will be higher than those in the first cavity. The second drift space has the same function as the first. This process continues in each following cavity up to the fifth cavity in this design.

In the last (fifth) cavity, the RF energy is extracted from the beam, allowed to travel through the uptaper section and then converted from the TE_{02} mode to a more versatile Gaussian-like mode, such as the HE_{11} mode using a mode converter. The mode conversion process happens in three steps. The Gaussian-like modes propagate through the corrugated transmission lines and windows with very low loss and low mode conversion compared to the TE_{mn} schemes [31].

The extraction cavity and uptaper must be very carefully designed to prevent mode conversion from the design mode to unwanted modes. Usually, a nonlinear uptaper is used to achieve this. Furthermore, this nonlinear taper must not allow RF oscillations to occur from the spent electron beam.

Finally, the spent electron beam will be collected in the collector region, where the beam dissipates on a water-cooled wall. The RF will reach the mode converter and then propagate through an oversized, low-loss corrugated waveguide to the application.

2.2.1 The RF Source

The low-power RF source must be able to supply approximately 50 mW CW with a bandwidth of greater than 1 GHz at a center frequency of 140 GHz. The source should also be capable of generating short pulses and be very phase stable. Possible systems include an IMPATT diode injection locked by a GUNN diode in a 4-phase pulse-forming network.

2.2.2 Superconducting Magnet

The high precision superconducting magnet for this experiment was requisitioned from Magnex Scientific, LLC. The maximum field strength is 6.2 T with a $\pm 0.5\%$ uniform length of 28 cm. The magnet has a 5-inch horizontal, room-temperature bore with a flange at one end for mounting the external, copper gun coil. A unique feature of this magnet is that it is actively shielded such that the magnetic field falls off as $B_z \sim 1/z^4$ in the vicinity of the cathode. Fig. 2-3 shows the predicted magnetic field profile along with the fall-off exponent of the field strength.

2.2.3 Power Supply

The power supply must be capable of supplying at least 15 kV at 0.15 A continuously and should be capable of millisecond-scale pulses. It may be necessary to have a power supply capable of microsecond-scale pulses. Furthermore, the unit should be capable of interfacing with a computer to facilitate automation and data acquisition.

2.3 Main Components

In the following chapters, the electron gun, cavity circuit and mode converter will be discussed in detail. These are the main components that require careful design in this project.
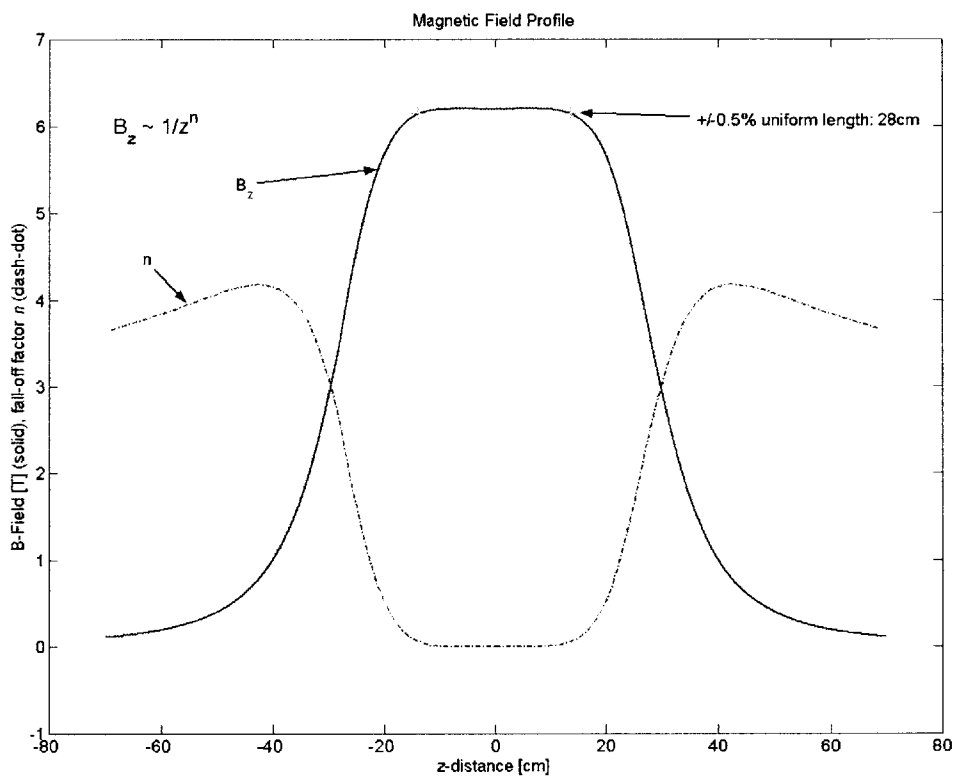
Figure 2-3: The predicted magnetic field profile shown at the rated maximum field strength of 6.2 T. The $\pm 0.5\%$ uniform field length is 28 cm and the field falls off as roughly $B_z \sim 1/z^4$ in the vicinity of the cathode, which is located at $z = -55\ cm$.

Chapter 3

Theory

In the first section of this chapter, first-order design equations are presented for electron gun design. The first-order design is an essential part of optimizing an electron gun. Next, the electron cyclotron interaction is explained and the gyroklystron theory is presented in its linear and non-linear forms. Lastly, the topic of mode conversion is discussed.

3.1   Magnetron Injection Gun

The Magnetron Injection Gun (MIG) is responsible for generating the high quality electron beam necessary for successful operation of the gyroklystron. Figure 3-1 shows a cross sectional slice of the electron beam and the typical electron orbit. Since the electrons do not cross the straight, axial magnetic field lines, θ_0 and r_g are essentially fixed for a given electron in a constant magnetic field. This means the current density is approximately constant throughout the length of homogeneity in the magnetic field. The Larmor radius along with other parameters used in this section are defined below in Sec. 3.1.2.

The characteristics of the electron beam are determined largely by the operation voltage, V_o, which controls the acceleration, and therefore the velocity, of the electrons as they are thermionically emitted from the cathode. The relativistic constant γ_o

33
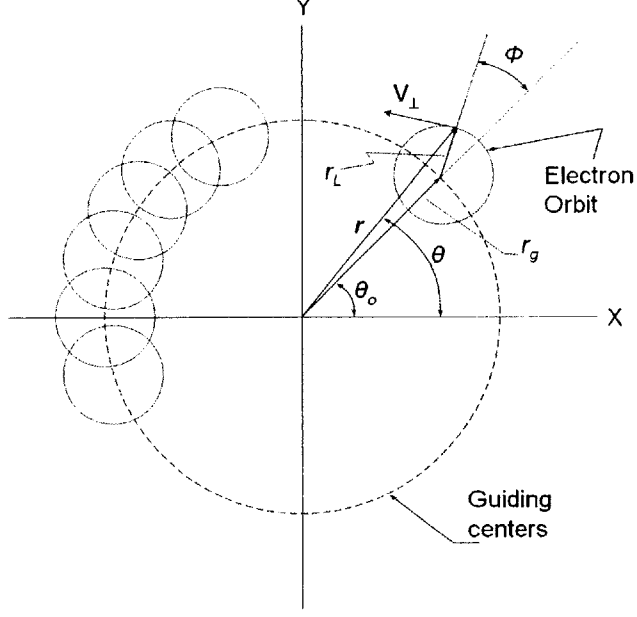
Figure 3-1: Diagram of beam cross-section showing the guiding center and Larmor radii.

relates V_o to the velocity components of the electron, $v_\perp$ and $v_\parallel$ as

$$\gamma_o = \left[1 - \frac{(v_\perp^2 + v_\parallel^2)}{c^2}\right]^{-1/2} \simeq 1 + \frac{V_o(kV)}{511} \tag{3.1}$$

where m_e is the electron mass and c is the speed of light. For a typical design voltage of around 60 kV, $\gamma_o \simeq 1.12$. The values for $v_\perp$ and $v_\parallel$ are obtained by using the definition of the pitch factor: $\alpha = v_\perp/v_\parallel$. The magnetic field controls the frequency at which the electrons orbit the magnetic field lines through the relativistic electron-cyclotron equation:

$$\omega_c = \frac{eB}{\gamma_o m_e} = \frac{v_\perp}{r_L} \tag{3.2}$$

where e is the charge of an electron and r_L is the Larmor radius at which the electron orbits around the magnetic field.

MIG designs are typically either diodes or triodes. In the triode configuration, there are two anodes (Fig. 3-2). The first anode is responsible for accelerating the

34
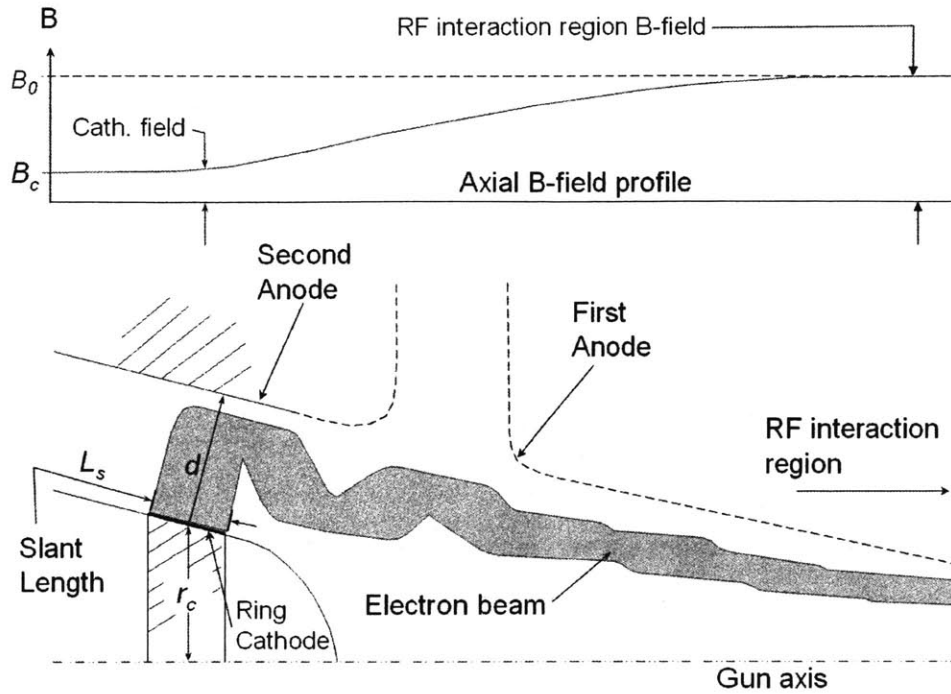
Figure 3-2: Diagram of the typical triode MIG showing the beam and two anodes.

electrons up to the desired relativistic level, while the second anode allows the user to tune parameters such as the pitch factor, α. In a diode configuration, the potentials on both anodes are the same and they are fabricated as one unit. The advantages of the diode configuration are that the power supply is much simpler and that there are fewer ceramic insulation rings, which can be a source of electrical breakdown problems and also drive up the cost and complexity. With a diode there also are fewer parameters to optimize in the experiment. In the case where tuning α is important, or where the electron beam requirements are such that the diode design does not meet the specifications well, then a triode structure must be used.

In MIG design, there are five primary parameters constrained by the requirements of the system and four free variables that must be optimized for any given set of primary parameters [32]. These parameters are listed in Tab. 3.1. Additional considerations beyond these nine key gun design parameters are the mode of operation in the tube, harmonic number, and magnetic field requirements or constraints.

35

Table 3.1: Key MIG design parameters

Parameter	Symbol	Design value
Beam power	$P_o = V_o \times I_o$	2.3 kW
Electron energy	γ_o	1.029
Cyclotron frequency	ω_c	$2\pi \times 140 \times 10^9\ rad/s$
Guiding center radius	r_{go}	0.64 mm
Pitch factor	$\alpha = v_\perp/v_\parallel$	1.5
Cathode Radius	r_c	4.02 mm
Cathode Current Density	J_c	2 A/cm^2
Cathode Slope Angle	ϕ_c	50°
Cathode-Anode Spacing Factor	D_F	3

While computer codes are very important in optimizing the electron gun design, it is important to start with a good first-order design. Typically, the most important parameter is the cathode radius, r_c. For some choices of variables, such as low voltages (corresponding to low γ_o), no suitable r_c exists due the presence of space charge.

Analysis for a first-order cavity design begins with the assumptions of cylindrically symmetric DC fields in the cavity, $\mathbf{E(r,z)}$ and $\mathbf{B(r,z)}$, as well as an assumption of conservation of momentum. To lowest order, $\mathbf{B(r,z)}$ can be assumed to be constant over the thickness of the electron beam, and thus becomes simply $\mathbf{B(z)}$, where the boldface indicates a vector quantity.

The following first order analysis for the MIG is presented in Baird, *et al* [32]. The fundamentals of MIG design are cast in a way that simplifies the design down to the four free variables that were listed in Tab. 3.1. The definitions for the parameters used in this section are defined below in Sec. 3.1.2.

Figure 3-3 shows the first order approximation of the electron gun as two concentric cones. The DC electric fields in this configuration are approximated by the equation for potential in a cylinder using a substitution to obtain the cones:

$$E(r) = \frac{-V_a}{r \ln(\ r'_a/r'_c\ )}$$

(3.3)

where $r'_c = \frac{r_c}{\cos(\phi_c)}$ and $r'_a = \frac{r_a}{\cos(\phi_c)} = r'_c + d$.

The spacing factor, D_F, is normally chosen to have a minimum limit of 2, where
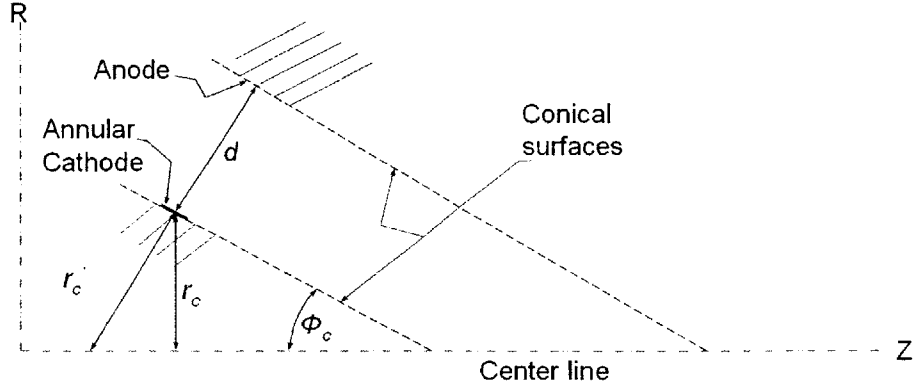
Figure 3-3: Diagram showing the definitions in a simplified system of conical electrodes.

the beam clears the anode wall by one Larmor diameter. D_F satisfies the following equation as a function of guiding center radius r_{go} and Larmor radius, r_L,

$$D_F = \frac{d\sqrt{r_{go}^2 - r_L^2}}{r_L r_{go}} \cos \phi_c \qquad (3.4)$$

Larger values of D_F give more clearance and also require higher second anode voltage. At the point where the first and second anode voltages are the same, the second anode becomes unnecessary.

The magnetic compression ratio, F_m, can be written,

$$F_m = \frac{B_o}{B_{zc}} = \kappa^2 R_c^2 \qquad (3.5)$$

The normalized slant length, L_s, and the normalized cathode radius, R_c, are related by,

$$\frac{L_s}{R_c} = \frac{I_o}{2\pi r_{Lo}^2 J_c} \frac{1}{R_c^2} \qquad (3.6)$$

The ratio of guiding center spread to guiding center is given by,

$$\frac{\delta R_g}{R_g} = \frac{\sin \phi_c}{\kappa^2 + 1} \frac{I_o}{2\pi r_{Lo}^2 J_c} \frac{1}{R_c^2} \qquad (3.7)$$

37

The cathode to anode spacing variables, D_{ac} and D_F are related to the cathode angle,

$$\frac{D_{ac}}{R_c} = \frac{D_F \kappa}{\cos \phi_c} \tag{3.8}$$

The normalized potential is given by,

$$\Phi_a = \frac{\ln(1 + D_F \kappa)}{\ln(1 + 2\kappa)} \left\{ \left[1 + \frac{4}{\kappa^2} \frac{\gamma_o^2 - 1}{R_c^2 \cos^2 \phi_c} \frac{\alpha_o^2}{\alpha_o^2 + 1} \left(\frac{1 + \kappa}{1 + 2\kappa} \right)^2 \right]^{1/2} - 1 \right\} \tag{3.9}$$

The electric field should never exceed approximately 100 kV/cm to prevent arcing, although the actual design may need to be much below this limit. The cathode nose is typically a point of high stress. One way to alleviate high electric field gradients is to increase the cathode radius, r_c. The possibility of arcing places a lower limit on r_c.

$$\frac{E_c}{E_{max}} = \frac{m_o c^2 / e}{E_{max} r_{Lo}} \frac{\Phi_a \cos \phi_c}{\ln(1 + D_F \kappa)} \frac{1}{R_c} \tag{3.10}$$

The ratio of beam current density to Langmuir limiting current density, J_c/J_L, must be kept below 15-20% because adiabatic MIG design assumes negligible effects of space charge. As r_c is increased, this ratio quickly increases, and this equation sets a hard upper bound on the size of r_c since it scales as approximately r_c^5:

$$\frac{J_c}{J_L} = \frac{2\pi r_{Lo}^2 J_c (1 + D_F \kappa) C_1^2}{14.66 \times 10^{-6} (m_o c^2 / e)^{3/2} \cos^2 \phi_c} \frac{R_c^2}{\Phi_a^{3/2}} \tag{3.11a}$$

$$C_1 = \exp(-C_2/2) \left[C_2 + \frac{1}{10} C_2^2 + \frac{5}{300} C_2^3 + \frac{24}{9900} C_2^4 + \ldots \right] \tag{3.11b}$$

$$C_2 = \ln(1 + D_F \kappa) \tag{3.11c}$$

where Eq. 3.11c is accurate to three significant figures up to $C_2 = 3.0$. If one finds the lower bound on r_c from (3.10) is greater than the upper bound from (3.11), then that MIG design might not be possible unless beam voltage is increased or α_0 is lowered.

The perpendicular velocity, can be approximated as follows for small cylindricity parameter, κ:

$$v_{\perp o} \approx \frac{F_m^{3/2} E_c \cos \phi_c}{B_o \gamma_o} \tag{3.12}$$

38

where the following relation also holds:

$$\frac{\Delta v_{\parallel}}{v_{\parallel}} = \alpha^2 \frac{\Delta v_{\perp}}{v_{\perp}} \qquad (3.13)$$

The assumption of adiabatic flow, meaning that the perpendicular energy of the electrons is proportional to $B(z)$, can be violated if the variations in the static electric or magnetic fields occur on a scale smaller than the gyro-orbit of the electron:

$$\frac{d}{dz}\{B, E\} \ll \frac{\{B, E\}}{z_L} \qquad (3.14a)$$

$$\frac{d^2}{dz^2}\{B, E\} \ll \frac{\{B, E\}}{z_L^2} \qquad (3.14b)$$

where z_L is the axial length travelled by the electron during one cyclotron orbit. In the vicinity of the cathode, care must be taken to form shapes that promote adiabatic flow. An elongated cathode nose is occasionally used to produce quick variations in E-field, but this can lead to large non-adiabatic effects.

3.1.1 Other Sources of Velocity Spread

Besides the velocity spread due to geometric optics, velocity spreads also occur due to thermal non-uniformity and roughness of the cathode surface. Estimates of these values are given by Tsimring [33]:

$$\left(\frac{\Delta v_{\perp}}{v_{\perp}}\right)_T = \left[\frac{KT_c}{m_o}\frac{F_m}{\gamma_o}\right]^{1/2}\frac{1}{v_{\perp o}} \qquad (3.15)$$

$$\left(\frac{\Delta v_{\perp}}{v_{\perp}}\right)_R = 0.4\left[\frac{2eE_cR}{m_o}\frac{F_m}{\gamma_o}\right]^{1/2}\frac{1}{v_{\perp o}} \qquad (3.16)$$

where K is Boltzmann's constant, T_c is the cathode temperature in Kelvin, and R is the radius of a small hemispherical bump characteristic of the cathode roughness. The spreads are estimates of the standard deviations of the velocities such that the average spread width would be given by $\pm(\Delta v_{\perp}/v_{\perp})$.

39

These spreads due to optical, thermal and roughness effects combine orthogonally,

$$\left(\frac{\Delta v_\perp}{v_\perp}\right)_{total} = \left[\left(\frac{\Delta v_\perp}{v_\perp}\right)_O^2 + \left(\frac{\Delta v_\perp}{v_\perp}\right)_T^2 + \left(\frac{\Delta v_\perp}{v_\perp}\right)_R^2\right]^{1/2} \qquad (3.17)$$

Generally, one can expect the total spread to be at least double that of the optical spread when the roughness and thermal spreads are included. The value of total perpendicular spread assumed for this design was 4% (parallel spread of 9%).

3.1.2 Variable Definitions for MIG design section

V_o = Beam voltage, volts

I_o = Beam current, amps

γ_o = $1 + eV_o/m_o c^2 \approx 1 + V_o(kV)/511 = relativistic\ mass\ factor$

v_o = $c(1 - 1/\gamma_o^2)^{1/2} = electron\ velocity,\ m/s$

v_{zo} = $v_o/(\alpha_o^2 + 1)^{1/2} = longitudinal\ velocity,\ m/s$

α_o = $v_{\perp o}/v_{zo} = pitch\ factor$

ω_c = $2\pi f_{co} = eB_o/m_o\gamma_o = relativistic\ cyclotron\ frequency,\ rad/s$

r_{go} = guiding center radius at RF interaction region, m

r_{Lo} = $v_{\perp o}/\omega_c = Larmor\ radius\ at\ RF\ interaction\ region,\ m$

R_g = $r_{go}/r_{Lo} = normalized\ mean\ guiding\ center\ radius$

δR_g = $\delta r_{go}/r_{Lo} = normalized\ full\ width\ guiding\ center\ spread$

κ = $(R_g^2 - 1)^{-1/2} = cylindricity\ parameter$

F_m = $B_o/B_{zc} = magnetic\ field\ compression\ ratio$

R_c = $r_c/r_{Lo} = normalized\ mean\ cathode\ radius$

ϕ_c = Cathode tilt angle (always positive)

L_s = $l_s/r_{Lo} = normalized\ slant\ length\ of\ cathode$

D_F = Cathode to Anode spacing factor (select $D_F \geqslant 2$)

D_{ac} = $d/r_{Lo} = normalized\ slant\ spacing\ between\ cathode\ and\ anode$

Φ_a = $eV_a/m_o c^2 = normalized\ first\ anode\ voltage$

E_c = Cathode electric field

E_{max} ≈ $10^7\ V/m\ as\ a\ conservative\ value$

J_c = Temperature limited cathode current density, A/m^2

J_L = Langmuir space charge limited current density, A/m^2

3.1.3 Computer Codes for MIG design

If J_c/J_L in Equation (3.11) seems questionably high, the self consistent MIG design codes will indicate whether there is a space charge problem or not. These codes typically do not, however, estimate the spread due to thermal non-uniformity or surface roughness, which must be considered separately.

Currently, there are several common MIG design codes available, such as several versions of EGUN [34], OMNITRACK (2D and 3D) [35][36], and MICHELLE [37]. EGUN was used extensively in the design of this MIG. These computer codes self-consistently compute the trajectories of the electrons as they propagate from the cathode down through the cavity region. In the problem of the moving charge, it is important to consider the self-consistent effects. Since the electron is a charge, it experiences forces from the electrostatic fields in its path and simultaneously alters them. Since it is also a moving charge, it generates a current of its own and therefore a magnetic field, which affects the total magnetic field it experiences. 2-D codes have been able to handle this just fine for over 20 years, but the newer 3-D codes require a lot of computer power to get a fine enough mesh and time resolution for the simulations. 3-D gun codes are gaining popularity in the multi-beam klystron (MKB) community, where it is very important to consider everything in the full three dimensions. 2-D gun codes are usually sufficient for present day gyro-devices, but 3-D codes can be used where it is desirable to simulate the effects of, for example, non-uniform cathode emission.

3.2 The Cyclotron Resonance Maser interaction

Once the electron beam has been generated, it is passed through a series of cavities where it interacts with RF fields in the cavities. In this section, we will consider the RF fields in the cavities and the phase space of the electrons (since we already determined that their position averaged over orbit is essentially fixed). Let us again

42
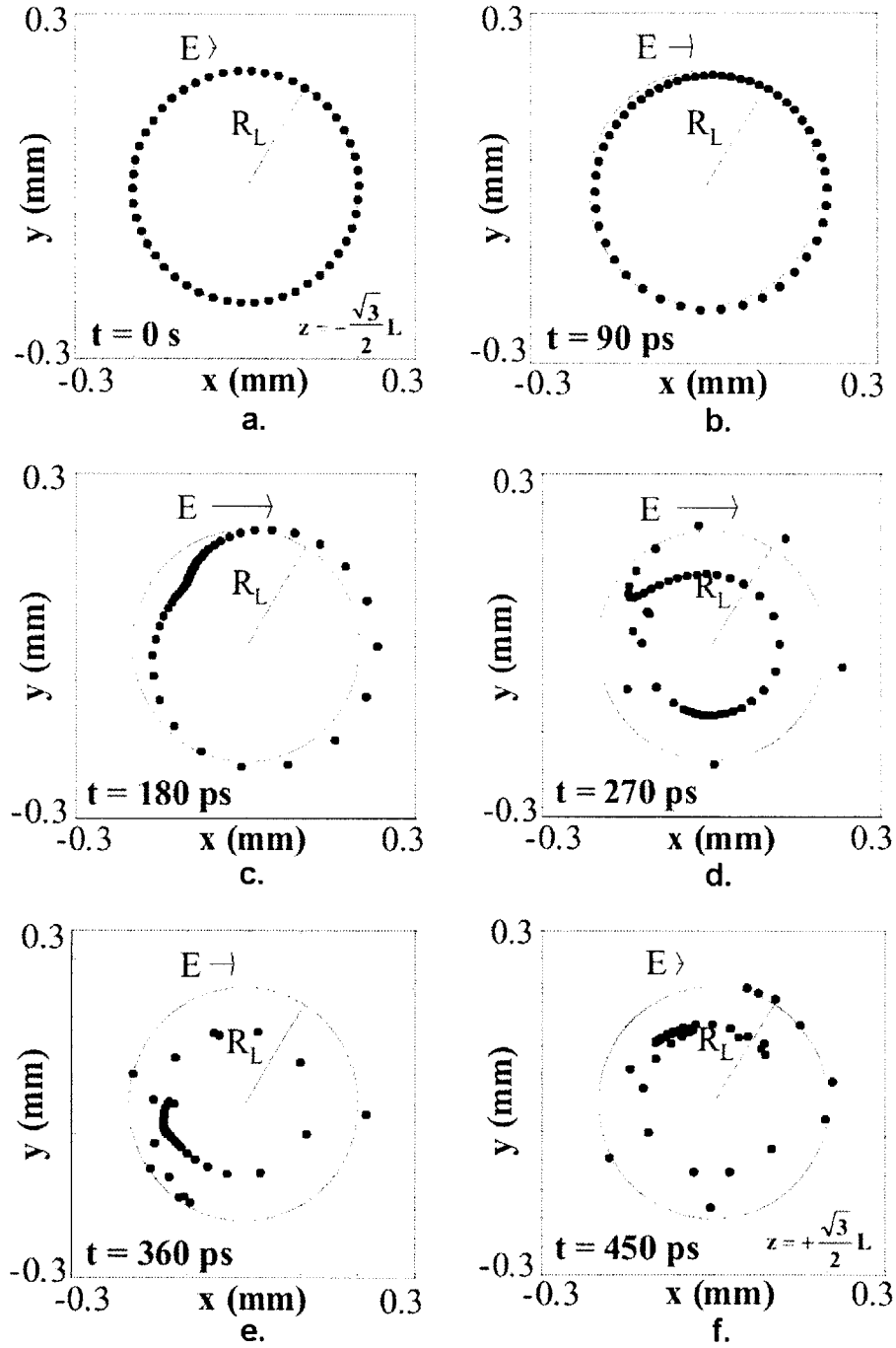
Figure 3-4: Evolution of electrons in phase space: (a) Initial uniform distribution of phases; (b) acceleration of electrons; (c-d) formation of the bunch and transfer of electron momentum; (e-f) spent beam. (Courtesy of J. Anderson)

consider the equation for electron-cyclotron frequency:

$$\omega_c = \frac{eB}{\gamma_o m_e} = \frac{v_\perp}{r_L}$$

Note that ω_c is inversely proportional to the relativistic mass, $\gamma_o m_e$. This is important, because the relativistic mass of the electron changes if the electron gains or loses energy. First, let us consider a beam travelling down a straight cylinder that supports the TE_{01} mode. Fig. 3-4 illustrates snapshots of the distribution of electron phases in Larmor space at 90 ps intervals as a beamlet interacts with RF energy. This figure shows essentially one beamlet with a distribution of electron positions around the central magnetic field line. Since initially there is no interaction and the electrons are uniformly distributed, each electron is equally spaced around a circle of radius equal to the Larmor radius, as in Fig. 3-4a. In (b), the RF electric field $\mathbf{E}$ begins to grow and exerts a force $\mathbf{F} = -e\mathbf{E}$ on the electrons, accelerating and decelerating electrons at the rate $\mathbf{F} \cdot \mathbf{v}$, which depends on the angle between $\mathbf{F}$ and $\mathbf{v}$. Since this is a relativistic beam, adding energy to the electron causes its mass to increase (or equivalently, the magnetic field it sees to decrease). For electrons with a larger mass, the Larmor radius now increases. For electrons that give up energy as RF, their relativistic mass decreases, so their Larmor radius decreases. This is especially evident in plot (c) where there is a high concentration of electrons (a "bunch") with a decreased radius, indicating that the electrons are losing a significant amount of energy. This is the goal of the bunching process and the main mechanism behind the CRM interaction. In (d), there is clearly a new, smaller Larmor radius almost concentric with the original Larmor radius. In (d) and (e), this smaller radius indicates a spent electron beam. In (f), the radii appear slightly enlarged, indicating that the electrons are again taking energy from the RF fields and the interaction is reversing.

Another important part of this CRM interaction is that the electron cyclotron frequency ω_c depends on the perpendicular velocity. As the RF fields alter the trajectories of the electrons, the cyclotron frequency changes. As the electrons lose relativistic energy, their electron cyclotron frequency increases. When velocity spread is

44

added to the picture, there is a spread of cyclotron frequencies that can excite multiple stagger tuned cavities in a gyroklystron and actually enhance the power output over a narrow range of frequencies.

Analysis of gyro-devices is usually done using a set of normalized variables. The normalized field amplitude in the cavity is defined to be μ, the normalized length of the cavity is F, and Δ is the detuning parameter defined by

$$\mu = \frac{\pi \beta_{\perp 0}^2}{\beta_{\parallel 0}} \frac{L}{\lambda} \tag{3.18a}$$

$$F = \frac{E_0 \beta_{\perp 0}^{n-4}}{B_0 c} \left(\frac{n^{n-1}}{2^{n-1} n!} \right) J_{m \pm n}(k_\perp r_b) \tag{3.18b}$$

$$\Delta = \frac{2}{\beta_{\perp 0}^2} \left(1 - \frac{n \omega_{c0}}{\omega} \right) \tag{3.18c}$$

where $\beta_\parallel = v_\parallel / c$ and $\beta_\perp = v_\perp / c$ are the normalized velocity components, L is the length of the cavity, E_0 is the field amplitude in the cavity defined in Eq. 3.24, n is the harmonic index (which will be assumed to be unity from here on), ω_c is the cyclotron frequency defined in Eq. 3.2, r_b is the radius of the electron beam and the subscript "0" denotes quantities at the entrance of the interaction region. The plus and minus signs on the Bessel function indicate asymmetric modes ($m \neq 0$) rotating in the same or opposite direction as the spiraling electrons, respectively.

Now, with a qualitative understanding of the bunching process, we can look at the governing equations of motion for the electrons. Under the assumption of a single-mode fundamental interaction and an approximation of weakly relativistic electrons ($\beta_\perp^2 \ll 2$), the so-called Yulpatov equations [38] reduce to the pendulum equations,

$$\frac{dp}{d\zeta} = -F f(\zeta) \sin \theta \tag{3.19a}$$

$$\frac{d\theta}{d\zeta} = -(\Delta + p^2 - 1) - F f(\zeta) p^{-1} \cos \theta \tag{3.19b}$$

45

where p, θ and ζ are given by,

$$p = \frac{\gamma \beta_\perp}{\gamma_0 \beta_{\perp 0}} \tag{3.20a}$$

$$\theta = \phi - \omega t_0 + \frac{\pi}{2} \tag{3.20b}$$

$$\zeta = \frac{\pi \beta_{\perp 0}^2}{\beta_{\parallel 0}} \frac{z}{\lambda} \tag{3.20c}$$

where ϕ is the fast time scale phase angle of the electron, t_0 is the time when the electrons enter the interaction region, and γ was defined in Eq. 3.1. $p(\zeta_{in}) = 1$ is the normalized momentum (assuming no velocity spread) and $\theta(\zeta_{in}) = \theta_0$, where θ_0 is uniformly distributed over $(0, 2\pi)$. In the final cavity, $\zeta_{in} = -\sqrt{3}\mu/2$ and $\zeta_{out} = \sqrt{3}\mu/2$ are typically chosen as the normalized input and output distances.

The $f(z)$ terms in Eqs. 3.19 and 3.22 are typically chosen to be a Gaussian field profile or a sinusoidal field profile. The Gaussian profile is used in the extraction cavity (last cavity) where the field leaks out toward the tube output. The sinusoidal profile goes to zero at $\zeta = \{0, \mu\}$ and so is used for closed cavities. The forms are as follows,

$$f(\zeta) = e^{-\left(\frac{2\zeta}{\mu}\right)^2} \tag{3.21a}$$

$$f(\zeta) = \sin\left(\frac{\pi \zeta}{\mu}\right) \tag{3.21b}$$

The electric fields in the cavity structure typically fall into two categories: Azimuthally symmetric TE_{0p} modes and whispering gallery modes of the form TE_{mp} where $m \gg p$ [2]. The TE_{0p} modes, where p is a low integer, like 1 or 2, are typically used in amplifier circuits because of low ohmic loss and a low presence of mode competition in the frequency spectrum. Over a fairly wide bandwidth, one mode can provide the needed power without losing power to different modes. Other modes, such as $TE_{2,3}$ or $TE_{21,13}$, for example, fall into the intermediate volume mode category. These modes fill the cavity, unlike the whispering gallery class, and may have even lower ohmic heating losses due to their more even distribution of fields. However, they are in a dense part of the mode spectrum, so techniques such as the use of coaxial

46

cavities are required to suppress mode competition.

The equations for electromagnetic fields in the gyroklystron cavity were derived in detail by Fliflet et al [39]. The slow time scale equation for an annular electron beam interacting with the circular TE_{mp} mode is given by

$$\mathbf{E}_\perp(r,\phi,z,t) = \mathbf{Re}\left\{ E_0 \left[J'_m(k_\perp r)\hat{e}_\phi + \frac{im}{k_\perp r}J_m(k_\perp r)\hat{e}_r \right] f(z)e^{i(\omega t - m\phi)} \right\} \quad (3.22)$$

where J_m is the Bessel function, $f(z)$ is the normalized axial RF field profile, and $k_\perp$ is the transverse wavenumber given by

$$k_\perp = \frac{\nu_{mp}}{R_0} = \sqrt{k^2 - k_z^2} \approx k \quad (3.23)$$

where ν_{mp} is the pth root of the Bessel function $J'_m(\nu_{mp}) = 0$ and R_0 is the cavity radius. The $\hat{e}_\phi$ component of the $\mathbf{E}_\perp$ field goes to zero in Eq. 3.22 at the cavity wall, and in the case of a symmetric waveguide mode of the form TE_{0p}, $J'_0(k_\perp r) = J_1(k_\perp r)$.

For a cylindrical cavity supporting the TE_{0p} azimuthally symmetric cylindrical waveguide mode, the field amplitude E_0 is calculated by integrating over the fields to obtain the energy. This equation, along with the equation for ohmic Q, allows us to find E_0 for a sinusoidal profile,

$$E_0 = \sqrt{\frac{Q_{tot(1)}P_{in}}{\omega\varepsilon_0\pi L}} \frac{2}{r_c|J_0(\nu_{0p})|} \quad (3.24)$$

where P_{in} is the input power to the first cavity, and Q_{tot} is defined as,

$$\frac{1}{Q_{tot}} = \frac{1}{Q_{ohmic}} + \frac{1}{Q_{diffractive}} \quad (3.25)$$

3.2.1   Linear Dispersion Relation

A linear dispersion relation for the RF/beam system can be derived if we ignore coupling between the beam and the RF waveguide modes. The RF modes in a

cylindrical waveguide produce the usual dispersion relation:

$$\omega^2 = c^2 k^2 = c^2(k_\perp^2 + k_\parallel^2) \tag{3.26a}$$

$$k_\perp = \frac{\nu_{mp}}{r_c} \tag{3.26b}$$

$$k_\parallel = \sqrt{k^2 - k_\perp^2} = \sqrt{\frac{\omega^2}{c^2} - \frac{\nu_{mp}^2}{r_c^2}} \tag{3.26c}$$

For gyro-devices, $k_\parallel$ is typically much smaller than $k_\perp$, so the waveguide resonant frequency is close to the cutoff frequency,

$$\omega_{res} \simeq c\frac{\nu_{mp}}{r_c} \tag{3.27}$$

The efficiency of the beam and RF interaction is strongest when the cyclotron frequency of the Doppler-shifted electron gyration is close to the resonant frequency of the waveguide. We can write this expression as the beam resonance condition,

$$\omega = n\omega_c + k_\parallel v_\parallel \tag{3.28}$$

where n is again the harmonic number. This relation is a straight line, as opposed to the waveguide dispersion relation, Eq. 3.26a, which has even symmetry and is quadratic (and furthermore depends on the mode). At the point where both of these lines intersect, an interaction takes place efficiently. Fig. 3-5 shows these relations plotted together.

3.2.2   Oscillation Start Current

If the electron-cyclotron frequency is close enough to the resonant frequency of the cavity, the presence of the electron beam can cause self-oscillations if the current is high enough. This is a serious problem for amplifiers, because the presence of oscillations not only causes the desired output spectrum to be polluted, but it also robs power from the frequency of interest, and can easily eliminate it completely. Therefore, it is important to avoid the onset of oscillations by adjusting the cavity

48
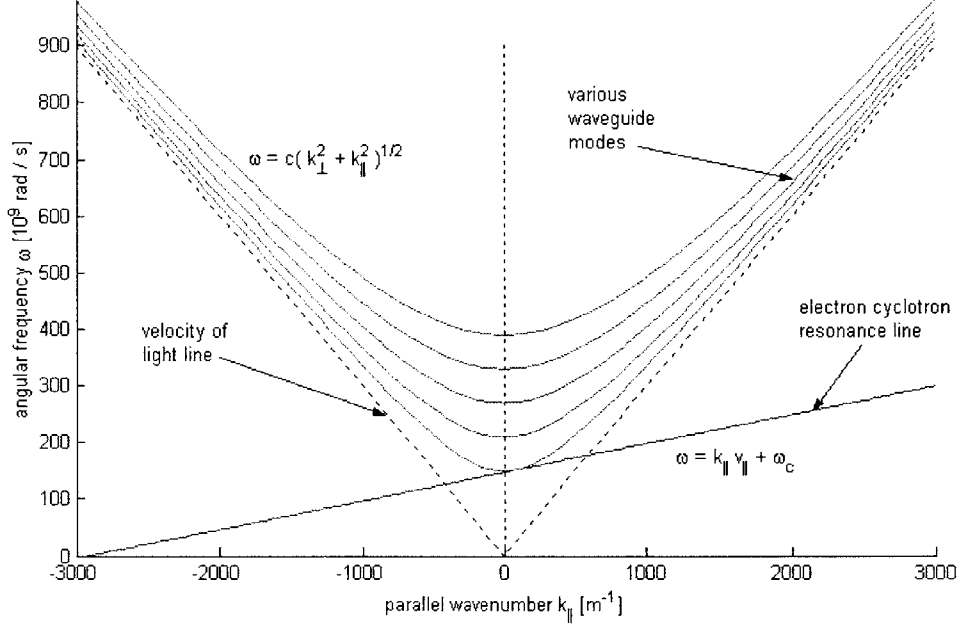
Figure 3-5: Uncoupled dispersion diagram for waveguide modes and resonance line.

dimensions, cavity Q's and the beam current. Here, the analysis adapted from Tran *et al* [18] is used.

The normalized current is typically used in gyro-device literature to describe the beam current, which takes into account the effects of the cavity Q, relativistic components, cavity length and the mode being supported. The normalized current is given (for the fundamental) by,

$$\hat{I} = \left(\frac{\sqrt{2}}{\pi^{5/2}}\right) \frac{I_A Q_{tot}}{c^3 m_e \varepsilon_0 / e} \frac{\beta_{\perp 0}^{-4}}{\gamma_0} \frac{\lambda}{L} C_{mp} \qquad (3.29)$$

where I_A is the actual beam current in amps. The constant $(\sqrt{2}/\pi^{5/2})$ in front of Eq. 3.29 is for a Gaussian profile. It becomes simply (π^{-2}) for a sinusoidal profile. The term C_{mp} is the coupling coefficient for mode mp given by,

$$C_{mp} = \frac{J_{m\pm 1}^2(k_\perp r_b)}{(\nu_{mp}^2 - m^2)J_m^2(\nu_{mp})} \qquad (3.30)$$

49

The normalized oscillation start current is defined by,

$$\hat{I}_{st} = \frac{4}{\pi\mu^2} \frac{e^{2x^2}}{\mu x - 1} \tag{3.31a}$$

$$x = \frac{\mu\Delta}{4} = \frac{\pi}{2\beta_{\|0}} \frac{L}{\lambda} \left(1 - \frac{\omega_c}{\omega_{mp}}\right) \tag{3.31b}$$

where μ and Δ are defined in Eqs. 3.18a and 3.18c, respectively, and the ω_{mp} term is the cutoff frequency in the waveguide for mode mp given by,

$$\omega_{mp} = c \left(\frac{\nu_{mp}^2}{r_c^2} + \frac{\pi^2}{L^2}\right)^{1/2} \tag{3.32}$$

The procedure for calculating the actual start current is to set the normalized beam current $\hat{I}$ equal to the normalized oscillation start current $\hat{I}_{st}$ and then solve for the actual current, I_A. We then get the equation,

$$I_A = C_0 \frac{c^3 m_e \varepsilon_0}{e} \frac{\beta_{\perp 0}^4 \gamma_0}{Q_{mp(tot)}} \frac{L}{\lambda} \frac{\hat{I}_{st}}{C_{mp}} \tag{3.33}$$

where C_0 is $(\pi^{5/2}/\sqrt{2})$ for a Gaussian profile or (π^2) for a sinusoidal profile. $Q_{mp(tot)}$ is the total Q factor for the mode mp in the waveguide defined by Eq. 3.25.

The diffractive Q factor is assumed large for a closed cavity where the only losses that exist are ohmic losses. For an open cavity, the diffractive Q is usually found from a cavity simulation code, preferably one that self-consistently includes the effect of the electron beam. The ohmic Q can be estimated by,

$$Q_{mp(ohmic)} \simeq \frac{r_c}{\delta} \left(1 - \frac{m^2}{\nu_{mp}^2}\right) \tag{3.34a}$$

$$\delta = \sqrt{\frac{2}{\omega\mu_0\sigma}} \tag{3.34b}$$

where δ is the loss tangent and the conductivity is $\sigma \approx 5.7 \times 10^7$ S/m for pure copper. In simulation, it is the conductivity value that is lowered to achieve a lower ohmic Q and therefore wider resonant cavity bandwidth. However, changing the conductivity of copper is usually not possible in the experiment, so lossy dielectric

inserts are typically placed in the cavity to lower the ohmic Q factor. The effects of the lossy dielectrics cannot be included in the present code, so they must separately be evaluated in an electromagnetic simulation program such as HFSS [40]. Lossy ceramic loads are not very desirable, so a more favorable method is lowering the total Q by cutting slots in the resonator that allow some of the fields to leak out and be absorbed outside the cavity. This latter method may also allow the cavities to be more accurately tuned in frequency and total Q.

For this experiment, only a lower-order mode is needed, so the start current profile is rather simple. Fig. 3-6 shows a sample oscillation start current plot for a cavity designed for the TE_{02} mode. Note that even though the TE_{02} mode start current crosses below the operating current of 65 mA, the magnetic field operating point (B_0) is such that oscillations will not occur. However, if for some reason the B_0 field must be lowered close to the 5 T point, oscillations may begin. The oscillation start current may be increased by lowering the Q and/or shortening the cavity length, L. The TE_{01} and TE_{22} modes cannot be excited because the operating magnetic field is too high. For this configuration, other modes, such as TE_{1p} had starting currents of over 2 amps.

3.2.3 Linear Theory

Using perturbation theory by expanding the momentum p and phase θ in the limit of small F parameter, we can linearize the pendulum equations presented in Eq. 3.19 for a simple two-cavity gyroklystron as follows,

$$p = p^{(0)} + p^{(1)} + \ldots \tag{3.35a}$$

$$\theta = \theta^{(0)} + \theta^{(1)} + \ldots \tag{3.35b}$$
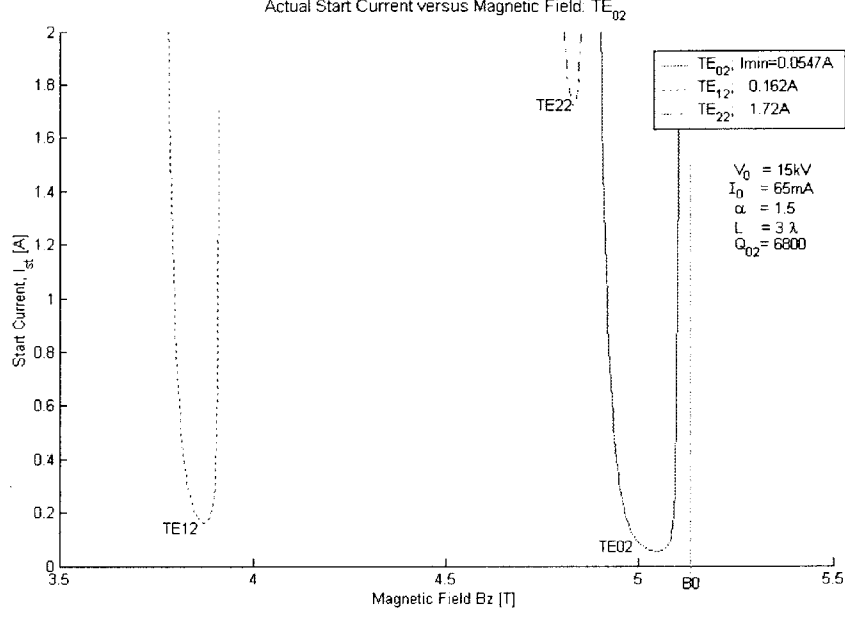
Figure 3-6: Plot of the oscillation start current versus B-field strength for various modes in a cavity designed to support the TE_{02} mode.

the equations become,

$$\frac{dp^{(0)}}{d\zeta} = 0, \tag{3.36a}$$

$$\frac{d\theta^{(0)}}{d\zeta} = -(\Delta + p^{(0)2} - 1), \tag{3.36b}$$

$$\frac{dp^{(1)}}{d\zeta} = -Ff(\zeta)\sin\theta^{(0)}, \tag{3.36c}$$

$$\frac{d\theta^{(1)}}{d\zeta} = -2p^{(0)}p^{(1)} - \frac{Ff(\zeta)\cos\theta^{(0)}}{p^{(0)}}, \quad \dots \tag{3.36d}$$

Solving these equations, integrating, approximating the result and making the assumptions that $|\mu x - 1| \ll 1$ and that there is no field in the drift spaces ($F = 0$), the analysis presented in [18] generalizes to an N-cavity gyroklystron as follows,

$$F_j = \frac{\sqrt{\pi}}{2} I \mu_j e^{-x_j^2} q_{j-1}(1 + \delta_j^2)^{-1/2}, \tag{3.37a}$$

$$\frac{q_j}{q_{j-1}} = \frac{\pi}{2} I \mu_j^2 \hat{\mu}_{d,j} e^{-2x_j^2}(1 + \delta_j^2)^{-1/2}, \quad j = 2, \dots, N-1 \tag{3.37b}$$

52

for beam current I, j^{th} normalized cavity length μ_j and parameter $\hat{\mu}_{d,j}$, detuning parameter Δ_j, parameter x defined by Eq. 3.31b and frequency pulling parameter $\delta_j = 2(\omega - \omega_0)Q_0/\omega$, where Q_0 and ω_0 characterize the unloaded cavity and ω is the working frequency in the loaded cavity. The definition for $\hat{\mu}_{d,j}$ contains the normalized j^{th} cavity length μ_j and the normalized j^{th} drift space length $\mu_{d,j}$,

$$\hat{\mu}_{d,j} = \frac{\sqrt{3}}{2}\mu_j + \mu_{d,j}, \tag{3.38a}$$

$$q_j = \sqrt{\pi}F_j\mu_j\hat{\mu}_{d,j}e^{-2x_j^2} \tag{3.38b}$$

Using this method, the q parameter is calculated in the first cavity and sequentially calculated for each following cavity until the extraction cavity is reached, where the linear theory usually begins to fail due to the nonlinear saturation.

3.2.4 Nonlinear Theory

When the phase difference between the electrons and RF fields is the appropriate value, a strong interaction takes place between them as described by the nonlinear pendulum equations, shown modified as,

$$\frac{dp}{d\zeta} = i(\Delta - 1 + |p|^2)p + iFf(\zeta), \tag{3.39a}$$

$$p(\zeta = \zeta_{in}) = e^{-i(\theta_{in})} \tag{3.39b}$$

with zero velocity spread initial conditions,

$$p_{in} = 1, \tag{3.40a}$$

$$\theta_{in} = \theta_c + q\sin\theta_c - \psi, \tag{3.40b}$$

where θ_c is uniformly distributed over $(0, 2\pi)$, and ψ is the RF phase in the cavity.

The perpendicular efficiency is defined by,

$$\eta_\perp(F, \mu, \Delta, q, \psi) = 1 - \int_0^{2\pi} |p(\zeta = \zeta_{out})|^2 \frac{d\theta_c}{2\pi} \tag{3.41}$$
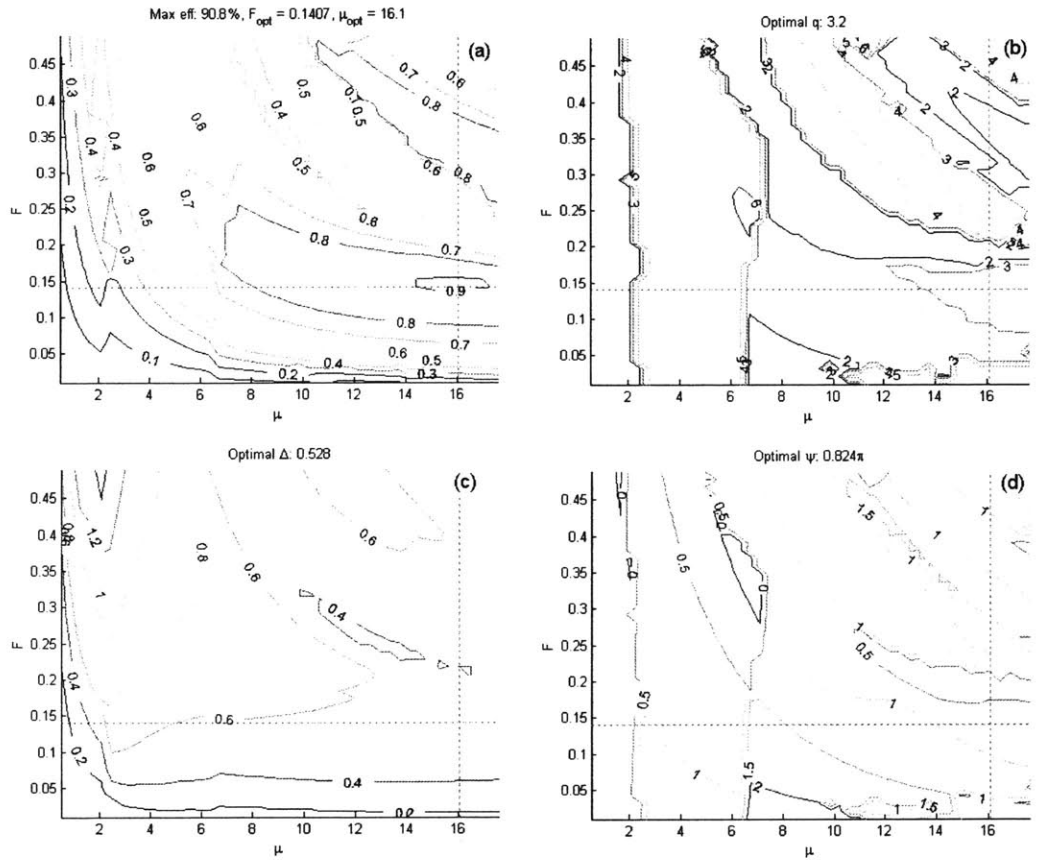
Figure 3-7: Efficiency contours of an optimized gyroklystron. (a) Optimized perpendicular efficiency $\eta_\perp$. (b) Bunching parameter q. (c) Detuning parameter Δ. (d) Relative phase ψ.

Applying an optimization for $\eta_\perp$ over q, Δ and ψ, the efficiency contours can be plotted versus μ and F, as shown in Fig. 3-7. The maximum perpendicular efficiency of 90.8% cannot be reached in a gyroklystron amplifier because it is in the oscillation regime. Furthermore, the optimal q value of 3.17 is difficult to reach for a low beam power gyroklystron, such as the one that will be presented here.

3.2.5 Computer Codes

Using the linear theory above, a code was written to get a basic understanding of the design fundamentals. The linear theory, however, turned out to be inadequate
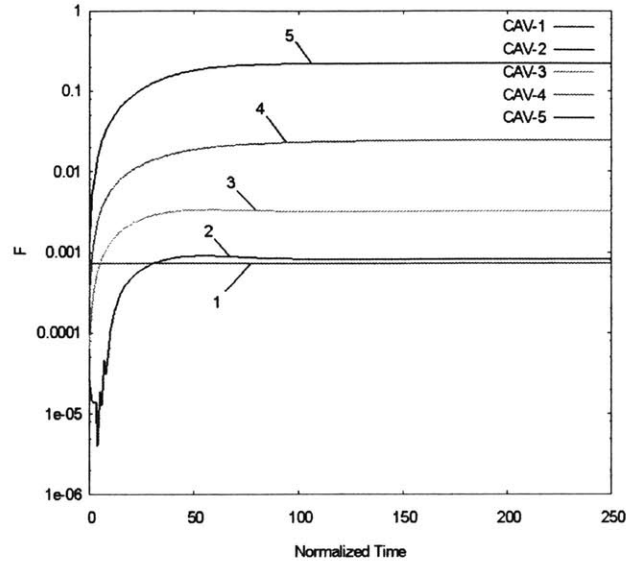
Figure 3-8: A sample output from a non-linear, non-stationary macroparticle code showing the temporal evolution of the fields in the cavity (Courtesy of J. R. Sirigiri).

for design, as several major assumptions are made, including zero field ($F = 0$) in the drift spaces, single mode and steady-state operation, validity of fluid theory and that self-consistent effects are negligible. Velocity spread was also not included. More detail on this linear code is presented in the next chapter.

Next a nonlinear, non-stationary code was written to solve the temporal evolution of the nonlinear pendulum equations for arbitrary shapes of longitudinal field profile in the cavity. This code included the effects of velocity spread by simulating a number of macroparticles with different initial momentum conditions separated into bins. A sample result of the temporal field evolution is shown in Fig. 3-8. This code does not calculate self-consistent effects and also assumes zero field in the drift section.

Several widely used simulation codes exist for modelling gyro-devices in various forms. MAGY is a self-consistent, time dependent code capable of modelling nonlinear and non-stationary, multi-frequency processes in slow and fast wave devices [41]. The code has been benchmarked against gyrotron and gyroklystron experiments and has shown excellent agreement. We have used MAGY for the design and optimization of our gyroklystron.

The sister code to MAGY is MAGYKL, which is specifically designed to model klystron and gyroklystron devices more quickly than MAGY while retaining simulation accuracy. MAGYKL is not self-consistent, and thus may not be a good choice for a TWT; but it is quite accurate for devices that utilize closed cavities.

Other codes for modelling gyro-devices include the two-dimensional MAGIC [42] and OOPIC [43], and the three-dimensional MAFIA [44] and ARGUS [45], which are all Finite-Difference Time-Domain (FDTD) particle-in-cell (PIC) codes. While we have access to MAGIC and OOPIC, we felt that the use of MAGY, a well established code, was sufficient for our design. The costly MAFIA and ARGUS codes were likewise not deemed necessary.

3.3 Mode Converter

Mode conversion is a very important matter in this project. In order to transmit the power from the gyro-amplifier to the existing 140 GHz DNP experiment, a low-loss, overmoded waveguide must be used. Such waveguides, however, support dozens of modes by their very nature of being overmoded. Hence having small perturbations in the waveguide wall, or bends of the waveguide, or different materials in the waveguide can cause mode conversion.

On this existing 140 GHz DNP experiment currently in place, there are three mode conversion steps to get to the desired HE_{11} mode. Two of the three mode conversion steps already exist and do not need to be designed here. Fig. 3-9 shows this three-step process: A circumferentially perturbed pipe converts TE_{02} to TE_{01}; A "snake" converter transforms TE_{01} to TE_{11}, and a scalar horn converts TE_{11} to HE_{11} before being transmitted through an overmoded corrugated waveguide. The latter two steps are already part of the experiment. The theoretical maximum efficiency for this whole process is 96.5%.
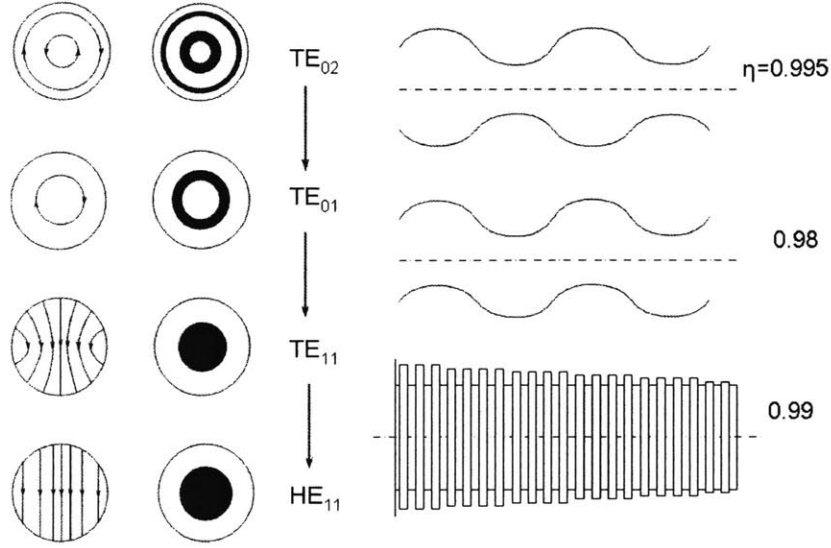
Figure 3-9: The mode conversion process: A circumferentially perturbed pipe converts TE_{02} to TE_{01}; A "snake" converter transforms TE_{01} to TE_{11}, and a scalar horn followed by overmoded corrugated waveguide converts TE_{11} to HE_{11}.

3.3.1 Theory

The first step of the mode conversion process is TE_{02} to TE_{01} and can be carried out by use of a mode converter with a periodically perturbed nonuniform waveguide wall of radius $a(z)$.

The following equation for the waveguide radius can be used to convert a TE_{02} mode into a TE_{01} mode, provided the converter radius is periodic with the beat wavelength $\lambda_B(2,1)$ of the two modes [46],

$$a(z) = a_0 \left[1 - \frac{\delta_0}{1 - \delta_0} cos\left(\frac{2\pi z}{\lambda_B} \right) \right] \qquad (3.42)$$

where p is the mode index, a_0 is the unperturbed cavity radius, δ_0 is the magnitude of the perturbations and

$$\Delta k_z = k_{z1} - k_{z2} = \frac{2\pi}{\lambda_B} \qquad (3.43)$$

where the k_z's are propagation constants for the two modes defined by,

$$k_{z1} = \sqrt{\left(\frac{\omega}{c}\right)^2 - \left(\frac{\nu_{01}}{a_0}\right)^2} \qquad (3.44\text{a})$$

$$k_{z2} = \sqrt{\left(\frac{\omega}{c}\right)^2 - \left(\frac{\nu_{02}}{a_0}\right)^2} \qquad (3.44\text{b})$$

where $J_0'(\nu_{0p}) = 0$ gives $\nu_{01} = 3.8317$ and $\nu_{02} = 7.0156$ for the TE_{01} and TE_{02} modes respectively.

The size of the perturbations is related to N by the equation,

$$\delta_0 N = \pi \frac{a_0^2 \sqrt{k_{z1}k_{z2}}}{\nu_{01}\nu_{02}d} = Constant \qquad (3.45)$$

where $d = 2\pi/\Delta k_z$ is the beat length and $z = Nd$ is the total length of the converter.

The length of the mode converter depends on the number N of beat period lengths used to obtain the desired conversion efficiency. Long converters are known for inherently narrow bandwidth, but short converters may suffer from poor conversion efficiency for certain mode conversion cases. In the case of TE_{02} to TE_{01} conversion, 99% conversion efficiency has been obtained with only two geometrical periods ($N = 2$) [47].

The bandwidth of a mode converter can be evaluated by introducing a detuning parameter $\Delta\xi(\omega)$ to the definition of Δk_z in Eq. 3.43 as follows,

$$\Delta\xi(\omega) = k_{z1}(\omega) - k_{z2}(\omega) - \Delta k_{z0} \qquad (3.46)$$

where Δk_{z0} is the difference of propagation constants at the design frequency and k_{z1} and k_{z2} are allowed to change simultaneously with frequency according to Eq. 3.44.

The efficiency as a function of detuning can then be derived,

$$efficiency = \alpha^2 \left(\frac{\sin\beta z}{\beta}\right)^2 \tag{3.47a}$$

$$\alpha = \frac{1}{2}\frac{\nu_{01}\nu_{02}\delta_0}{a_0^2\sqrt{k_{z1}k_{z2}}} \tag{3.47b}$$

$$\beta = \sqrt{\alpha^2 + \frac{\Delta\xi^2}{4}} \tag{3.47c}$$

Results of this theory along with simulation results are presented in Chap. 6.

A snake converter, such as the existing one in use in the DNP experiment, can be designed using a non-axisymmetric mode converter consisting of sections of constant radius of curvature periodically perturbed in one plane. In this case, we are trying to convert TE_{01} to TE_{11}. The equation for the waveguide radius coordinate is given by Thumm [47],

$$a(z,\beta) = a_0[1 + [\delta_{11}\cos\left(\Delta k_{zw}(01,11)\cdot z\right) - \delta_{12}\sin\left(\Delta k_{zw}(01,12)\cdot z\right)$$
$$- \delta_{21}\sin\left(\Delta k_{zw}(11,21)\cdot z\right)]\cos\beta] \tag{3.48}$$

where $\beta = \{0,\pi\}$ is the azimuthal angle in the perturbed plane and the δ's are perturbation coefficients.

3.3.2 Computer codes

CASCADE is a commonly used, powerful mode analysis software and can be used to optimize uptaper sections for minimal mode conversion [48]. For this project, CASCADE was used to predict the behavior of the nonlinear uptaper and of the TE_{02} to TE_{01} mode converter.

3.4 Discussion

In this chapter, an overview of the gyroklystron operation theory was given that focused on the electron gun (MIG), cavity structure and mode converter.

In the first section, the details of the Magnetron Injection Gun operation were discussed including different types of MIGs and their tradeoffs. Following that, the details of a first-order MIG design were presented. The topic of velocity spread was covered including its optical, thermal and roughness constituents. Several computer codes were introduced as an aid to MIG design.

Next, the CRM interaction was discussed in detail, including a qualitative interpretation of the bunching process. The common normalized parameter formalism was introduced and the equations of motion were presented. The electric field components and profiles were discussed along with the Q parameters. A linear dispersion relation was constructed to illustrate the interaction of the waveguide modes with the electron beam. The important self-oscillation start current was discussed and several methods of how to avoid oscillations were presented. A linear theory for the gyroklystron was presented followed by a nonlinear theory that led to efficiency optimization. Several computer codes were discussed including two unpublished independent codes.

Finally, the topic of mode conversion theory was introduced and the equations resulting from a simple mode converter theory were presented.

Chapter 4

The Gyroklystron Cavity Circuit

In this chapter, the design of a gyroklystron amplifier cavity circuit is described in detail. First, an overview of the gyroklystron cavity is presented followed by the criterion for mode choice, the design of the cavity and its characteristics, a preliminary design of the input coupler, and the conclusions.

4.1   Gyroklystron Amplifier Design

The choice of a gyroklystron design was motivated in part by a lack of other successful amplifier tubes at low beam voltage and current. The gyroklystron promised high gain per cavity and stability against oscillations that were not guaranteed in other devices such as the gyro-TWT. The main challenges in the gyroklystron were getting a high gain-bandwidth product in a device of very low beam current and voltage.

The basic concept of the gyroklystron is that a small RF signal is coupled into the first cavity. In this design, we have assumed that around 25 milliwatts (mW) will be coupled into the first cavity from an external source. These fields cause the electron bunching process to begin in the first cavity, as outlined in Chap. 3. In each of the following cavities, the stronger bunching strengthens the electric fields until the last cavity where the power is extracted out by diffraction. Fig. 4-1 shows a 5-cavity structure with evolving electric fields. The cavities are separated by drift spaces, which are ideally cutoff to the RF fields in the cavities so that no coupling
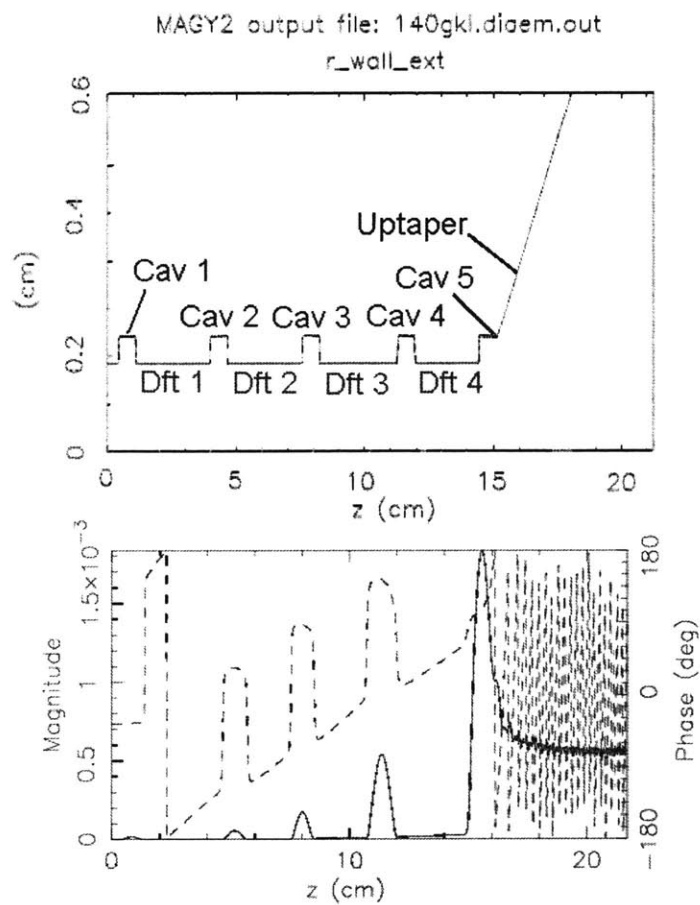
Figure 4-1: Profile of a 5-cavity gyroklystron with a linear uptaper section (top), Evolution of electric fields in the cavities (bottom).

occurs between cavities. In these drift spaces, the bunching continues to evolve in the near-absence of electric fields. Between cavities 4 and 5, a small electric field leakage can be seen in the drift space. The leakage is present because of evanescence and because the drift spaces are not perfect conductors. The presence of this leakage, along with several other factors, make the dynamics of the evolution too complicated to predict analytically, so computer codes are required for accuracy.

The drift spaces require special attention to ensure that unexpected modes are not excited. The ideal drift space should prevent RF modes from being sustained. Usually, a lossy dielectric is used to line the tube, but this actually opens the possibility of exciting hybrid modes, such as HE_{11}, HM_{11}, HE_{12}, etc. [23], which contain a mixture of both E_z and H_z components, since the propagation constant becomes complex $\beta = k_z - ik_{zi}$. Other modes, such as TE_{11}, TM_{11} and TE_{12} must also be considered. One method to verifying the desired operation is to evaluate the Qs of these modes against the beam current to ensure that oscillations will not occur [49].

The design sequence was as follows: An operating mode was chosen, the number of cavities and their dimensions were chosen based on linear theory, and the cavity circuit was modelled and optimized using the MAGY code. A description of these stages follows.

4.2   Mode of operation

The choice of operating mode is driven by ohmic wall losses, mode competition and feasibility of the electron gun cathode design. The coupling coefficient between the electron beam and RF fields in the cavities is given by,

$$C_{mp} = \frac{J_{m\pm1}^2(k_\perp r_b)}{(\nu_{mp}^2 - m^2)J_m^2(\nu_{mp})} \tag{4.1}$$

where the variables are the same as defined in Chap. 3. Since only azimuthally symmetric modes ($m = 0$) were considered, we only needed to choose between TE_{0p} modes, where $p = 1, 2, 3, \ldots$ Tab. 4.1 lists the coupling coefficients for several az-

63

Table 4.1: Coupling Coefficient C_{mp} for TE_{0p} modes

m p	Radial Maximum: 1	2	3	4	Cold cav radius (mm)
0 1	0.1422				1.31
0 2	0.0764	0.0270			2.40
0 3	0.0525	0.0186	0.0116		3.48
0 4	0.0400	0.0142	0.0088	0.0064	4.56
0 5	0.0323	0.0114	0.0071	0.0052	5.64
$R_b(mm)$:	0.63	1.82	2.92	4.01	

imuthally symmetric TE_{0p} modes, showing the quick decrease in coupling as the radial mode index p is increased and as the electron beam is placed further from the most central Bessel maximum. Thus the lowest order mode should be chosen with the TE_{01} mode being the most efficient in terms of beam to RF coupling. However, for a given beam current, the lower order modes require a smaller beam for a given frequency and smaller cavities. The beam is focused by the magnetic compression factor $F_m = B_o/B_{zc}$ introduced in Chap. 3, which is typically on the order of 30. The size of the electron gun cathode is limited by this magnetic compression factor, by current density and by space charge, so the beam cannot be made arbitrarily small. Furthermore, small cavities have much smaller surface areas, so ohmic heating can become a problem in these cases. The electron beam radii R_b are shown in Tab. 4.1 along the bottom and the cold cavity radii for several low order TE_{0p} modes are shown in the far right column. For example, if one chose the TE_{03} mode, where the beam is typically placed at the second Bessel maximum, the electron beam radius would be 1.82 mm, the coupling coefficient would be around 0.019 and the cold cavity radius would be 3.48 mm at $f_0 = 140\ GHz$.

4.2.1 Electron Gun Cathode

The average cathode radius r_c (defined in Chap. 3) is related to the beam radius r_b by the magnetic compression as $r_c = r_b\sqrt{F_m}$. If this average radius is too small, the slant length of the cathode will have to increase to meet the current density

requirement, driving the velocity spread up. Hence it is desirable to choose a higher order Bessel maximum to alleviate this consequence. Using higher Bessel maxima, however, results in lower coupling efficiency and may place the beam too close to the wall.

4.2.2 Cavity Heating

Another consideration in choosing the mode of operation is the ohmic heating of the cavity walls. In a relatively low power system such as this one, ohmic heating on the cavity walls is fairly small. The reason for this is somewhat hidden: In simulations we arbitrarily alter the Q value by essentially lowering the conductivity of the copper. In reality, this artifice is abandoned because it is impractical to change the copper conductivity; instead, the total Q is lowered by either introducing lossy ceramic inserts into the cavity (lowering the ohmic Q), or by cutting leaky slots in the wall to lower the diffractive Q. Since the ohmic Q is very high (low loss), the copper ohmic heating is small. If the total Q is lowered by diffraction, the absorbers outside of the cavity will have to handle the power dissipation. Fig. 4-2 shows the two methods for altering cavity Q pictorially.

In a PBG structure, however, the wall heating can become more important, as surface area of the rods is much smaller than the surface area of a pure cylinder. Due to the complexity of the field distributions in a PBG structure, the heating must be evaluated by observing the field intensities predicted by simulation. Fig. 4-3 shows a possible confinement of the TE_{02} mode in a PBG structure. The TE_{04} mode was also well confined, but the TE_{03} mode did not lay well in the triangular lattice structure.

4.2.3 Mode Conversion

In the most attractive mode conversion methods for us, higher order modes are likely to be converted to the TE_{01} mode before being converted to the Gaussian-like HE_{11}. It is rather easy to convert the TE_{02} mode to the TE_{01}, so it is again advantageous
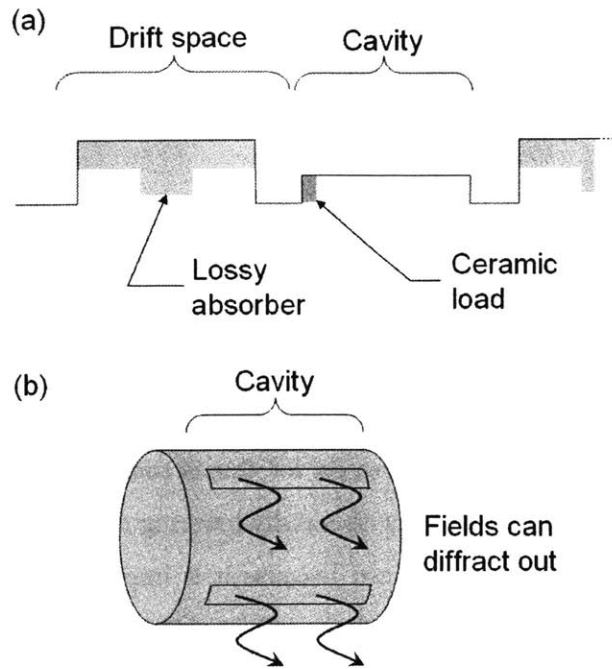
Figure 4-2: Two methods for lowering the cavity total Q: (a) loading the cavities with lossy ceramic inserts to lower the ohmic Q, (b) lowering diffractive Q by leaky slots.
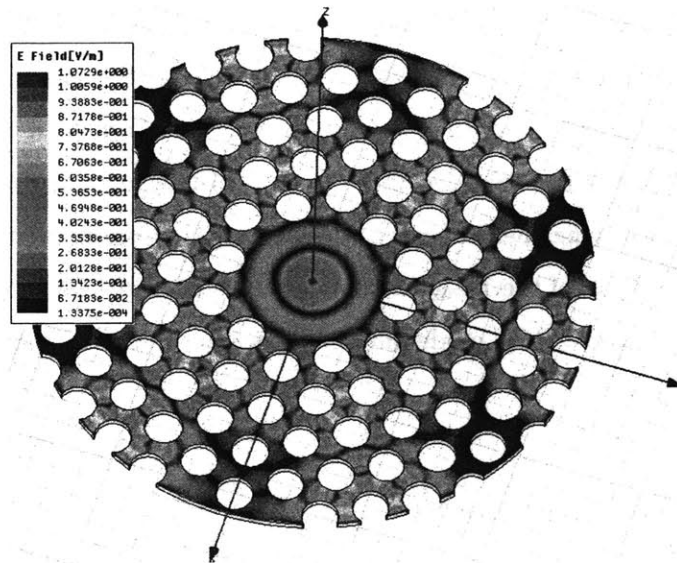
Figure 4-3: An HFSS simulation of a PBG structure to confine the TE_{02} mode. (Courtesy of J. R. Sirigiri)

to choose a low order mode, like TE_{02}. Higher order modes can be strongly coupled to other unwanted modes, often requiring longer mode converters that restrict bandwidth.

4.2.4 Mode Selection

The TE_{02} mode was chosen as the operating mode because it appeared to be a reasonable compromise between the design parameters and their tradeoffs. The fairly high coupling coefficient, lower ohmic losses, possible PBG mode confinement, feasible cathode design and lower sensitivity to machining tolerances were some of the benefits that the TE_{02} mode had over other modes.

4.3 Cavity Circuit

The cavity circuit design was done in stages. First, linear theory was used to get a rough idea of the behavior of the system, then the circuit was optimized using the MAGY simulation code. Tuning the uptaper section and output cavity required the use of a cold cavity code to predict the resonant frequency and Q.

4.3.1 Number of Cavities

Using a simple code based on the linear theory equations from Sec. 3.2.3, Fig. 4-4 was produced, which shows around 40 dB of unsaturated, linear gain using 5 cavities resulting in a normalized field amplitude of around $F = 0.04$, corresponding to an output power of around 150 W for cavity lengths of $3.5\lambda_0$ and Qs of 1000 each with a 15 kV, 65 mA beam at $\alpha = 1.5$ and an input power of 15 mW. The drift spaces were each $8.0\lambda_0$ long and the effects of velocity spread were not included. Based on this model, a 5-cavity gyroklystron was chosen as the starting point. A gyroklystron consisting of more than five cavities would be too difficult to construct and tune, so five was kept as the maximum number of cavities.
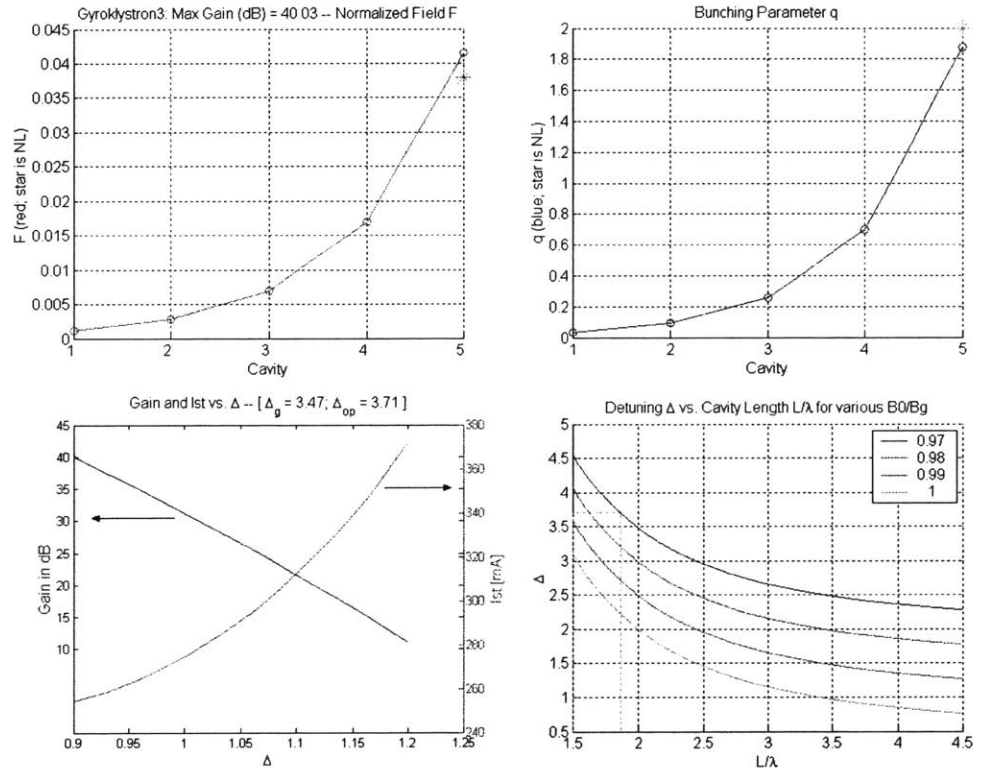
Figure 4-4: Output from an independent code based on linear theory showing target unsaturated gain of around 40 dB obtained with 5 cavities and cavity field amplitude $F = 0.04$.

4.3.2   Initial Cavity Dimensions

The TE_{02} mode required a cavity radius of 2.4 mm and the linear theory predicted reasonable results using cavity lengths of $3.5\lambda_0$ and drift section lengths of $8\lambda_0$. The linear code, however, assumes no fields in the drift section, so the radii of the drift sections are inconsequential.

4.3.3   Optimizing Cavity Circuit

The cavity optimization took place in several steps. Several parameters were at first assumed or roughly estimated and then later found more precisely. The initial design was based on linear theory results, but was not very realistic in terms of some of the parameters chosen.

A strategy had to be developed in order to perform this optimization. The outputs from MAGY show the electric field profiles in the cavities and the power in the cavities. Due to the delicate nature of the electron phases, in some cases, decreasing the electric field in the first few cavities actually caused an increase in predicted output power, and vice versa. Therefore, the strategy of maximizing the electric fields in the cavities was taken. This procedure was performed from the first cavity to the last cavity, since the electron beam travels in this manner.

To greatly ease the difficult and messy process of changing each parameter by hand, which would have been a prohibitively tedious task for evaluating bandwidth, MATLAB scripts were used to adjust the parameters of the input file, run MAGY, and collect and display the results. This method allowed an overlaying of a series of the important results due to parameter adjustments on one graph, making it much easier to pick a more favorable configuration. At the press of a button, difficult calculations requiring dozens of MAGY runs, such as evaluating bandwidth, could be performed easily, although it could still take several hours to get the result. Furthermore, once it was determined that MAGY's time-step parameter governing resolution could be relaxed and the number of simulation steps could be greatly reduced without loss of accuracy, it was possible to run MAGY at literally ten-times the previous speed. The

69

peak rate at which MAGY had been run to optimize this cavity circuit is estimated to be up to 5000 times per week! The total number of runs probably approached 50,000.

Once a stable design had been reached with very little or no stagger tuning, it was found that bandwidth and gain could increase simultaneously by increasing the cavity Q's. The cavities start to saturate from the center frequency outward, so the outer band edges benefit from increased gain while the center stops growing due to saturation. At some point, oversaturation sets in and the output power at the center frequency begins to decrease with further increases in gain or input power. At this point, we began stagger tuning the cavities to relieve the regions of oversaturation and spread the gain out more evenly. At first, this concept didn't seem to work as both power and bandwidth plummeted, but eventually it began to work as the right magnetic field and tuning patterns were found. After each few tuning steps, checking for oversaturation (varying input power) or scanning the magnetic field to make sure it was the optimal value were required operations. This was a lengthy process that required much trial and error. The cold-cavity resonant frequency of a cavity is around 400 to 500 MHz lower than the "hot" frequency, so figuring out which cavity was the cause of a feature of the frequency response was not always straightforward. Furthermore, each cavity's tuning frequency, Q and length contributed to the whole frequency response plot, so that none of the cavities had an independently variable contribution.

A brief discussion of the early stages of the design process follows. Next, three designs are shown below highlighting major milestones in the optimization of the cavity circuit: First, a low beam power circuit ($I_0=65$ mA) was designed that achieved 660 MHz bandwidth at 43 W, which seemed to be the limit for that beam current. Increasing the beam current increases the gain significantly, which helps get more power in the band edges, thereby increasing bandwidth and power. Thus the beam current was increased to 100 mA to yield a 920 MHz, 51 W design. Finally, the beam current was increased to 150 mA and stronger stagger tuning was used, which resulted in a 130 W output with almost 1.1 GHz bandwidth, theoretically exceeding

70

Table 4.2: Initial Design Parameters

Operation Voltage, V_0	15 kV	Cavity Length	3λ
Beam Current, I_0	0.065 A	Drift length	8λ
Pitch factor $\alpha = v_\perp / v_\parallel$	1.5	Cavity radii	2.4 mm
Design Mode	TE_{02}	Drift space radii	1.2 mm
Input Power, P_{in}	5 mW	Cavity ohmic Qs	all 1000
Magnetic Field, B_0	5.1 T		
Output Power	32 W	Bandwidth	375 MHz
Saturated Gain	38 dB		

the required specifications.

4.3.4 Initial Designs

The initial parameters chosen for the initial designs are shown in Tab. 4.2 and were based on linear theory. Initially, MAGY predicted no gain in the gyroklystron based on some of these parameters. The cavity radii were too large for the CRM interaction to occur and it took several dozen MAGY runs before any gain was found. The reasons for the difficulty in finding a suitable set of operating parameters are that MAGY is self-consistent and makes no assumptions about the fields in the drift spaces and that the presence of the electron beam causes a frequency upshift of 400 to 500 MHz in the cavities not predicted by linear theory, hence the cavity sizes and drift space lengths had to be sequentially modified from the simple linear theory.

Initially, the cavity lengths were held constant while the cavity radii were adjusted for maximum electric fields. The drift lengths were thought to be rather long at around $8\lambda_0$ each. The result (as shown in Tab. 4.2) was 38 dB of gain at an output power of around 32 watts and bandwidth of 375 MHz. However, a major problem with this design was that the drift space radii were not sufficiently large for the electron beam, which should be a minimum of three Larmor radii away from the electron beam guiding centers. Smaller drift space radii resulted in significantly higher gain, according to MAGY. Furthermore, when the input power was increased, the electrons became over-bunched, resulting in less output power as the input power increased.
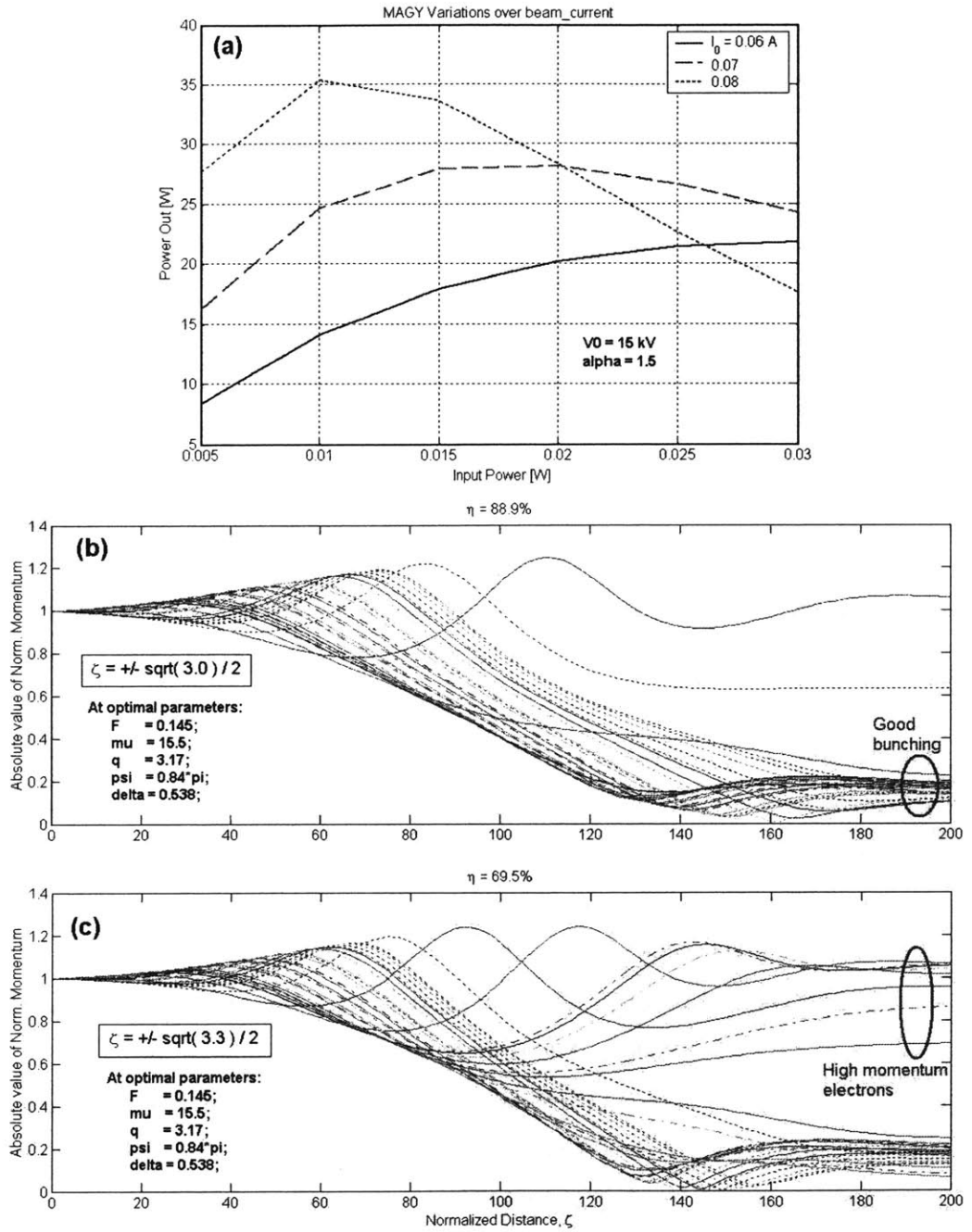
Figure 4-5: (a) Characteristic power saturation and over-saturation; (b) optimal saturated electron bunching and (c) over-bunching due to an elongated structure.

72

Fig. 4-5 illustrates the concept of the power saturation and over-saturation as well as the electron bunching process at saturated bunching and at over-bunching. In Fig. 4-5a, as the input power was increased, the result was a decreasing of the output power at higher beam current (design parameters are in Tab. 4.2). This can be explained as follows: The input power causes the electrons to bunch more quickly initially and the bulk of the electrons have lower momentum as they advance in the ζ-direction, but eventually many electrons regain momentum as a result of the CRM interaction and the result is a high average momentum, meaning the electrons have not given up the maximum amount of their energy. The same effect occurs if the structure is too long: Fig. 4-5b shows optimal gyrotron bunching using the normalized optimal positions $\zeta = \pm\sqrt{3}/2$ at the input and output of the interaction region, resulting in few high momentum electrons and maximum efficiency. As the length is increased slightly to $\zeta = \pm\sqrt{3.3}/2$ in Fig. 4-5c, the high momentum electrons reappear, resulting in a reduction of output power. Maximum output power represents maximum momentum loss in the electrons on average.

4.3.5 First Design

The next adjustments were increasing the drift space radii to three times the Larmor radius plus the beam guiding center radius, increasing the input power to a more reasonable 25 mW, lowering the ohmic Qs to increase the bandwidth, and optimizing over all dimensions of the cavity circuit: cavity radii, cavity lengths and drift space lengths. This procedure is rather time consuming, as only one parameter can be adjusted for a given simulation run. Typically, the cavity lengths were fixed based on the oscillation start current. The first cavity was then optimized for electric field strength, followed by the first drift space length, then the second cavity, etc., ending with the last cavity and the uptaper, which were both maximized for power. After performing this process several times and also readjusting the reference frequency and magnetic field, the gain usually went over 30 dB saturated. Tab. 4.3 shows the results of a 15 kV, 65 mA design achieving a saturated gain of 32 dB and a bandwidth of 660 MHz (with no velocity spread). This design is pushed to the limits by exploiting

Table 4.3: First Design Parameters

Operation Voltage, V_0	15 kV
Beam Current, I_0	0.065 A
Pitch factor $\alpha = v_\perp/v_\parallel$	1.5
Design Mode	TE_{02}
Input Power, P_{in}	25 mW
Magnetic Field, B_0	5.11 T
Output Power	43 W
Bandwidth	660 MHz
Saturated Gain	32 dB

	Length(λ_0)	Radius(mm)	$f_0(GHz)$	Q_{ohm}	Q_{diff}
cav1	5.5	2.401	139.9	800	800
dft1	9.9	1.85			
cav2	5.5	2.410	139.8	500	
dft2	9.8	1.85			
cav3	5.5	2.410	139.8	500	
dft3	9.2	1.85			
cav4	5.5	2.410	139.8	500	
dft4	11.1	1.85			
cav5	5.5	2.401	139.9	1200	660
upt	16.3				
dft5	12.6	4.0			

saturation to widen the bandwidth and increase the power output by increasing the cavity Qs. This is an unusually wide bandwidth and high gain for a gyroklystron operating at such low voltage and current.

4.3.6 Second Design

In order to get more gain to allow for mild stagger tuning, the beam current was increased to 100 mA. The new design parameters are shown in Tab. 4.4. With the new higher value of current, high gain was possible, but it was necessary to alter the cavity Qs to push the saturation. If the cavity Qs are carefully adjusted, it is possible to widen the bandwidth and increase the output power simultaneously by exploiting saturation. To evaluate the bandwidth for a certain set of parameters, MAGY must be run typically a dozen times even for a rough resolution. Hence it becomes very time consuming to evaluate more than a small portion of parameter space. However, with enough work, the bandwidth and power levels slowly increased.

4.3.7 Unusual effects of Q and velocity spread

The results in Tab. 4.4 show a bandwidth of 918 MHz at 51 W with no velocity spread. Firstly, the higher cavity Q's drive the gain up on the band edge while the center frequencies tend to saturate. This widens the 3 dB bandwidth in a somewhat counterintuitive way, since high Q's are normally associated with narrow bandwidth. Secondly, since this design had a large amount of oversaturation to widen the bandwidth, the velocity spread has the effect of relieving the oversaturation and producing higher power in the oversaturated region. This is very interesting because we are used to seeing only detrimental effects arising from velocity spread.

Fig. 4-6 shows one such plot whereby velocity spread up to 6% seems to help the power output. With velocity spread, there are some electrons with lower $v_\perp$ and higher $v_\parallel$ and vice versa, such that the relativistic γ_o is conserved. With differences in cyclotron frequency, and an array of resonant cavities tuned to different frequencies, it is possible to excite multiple cavities and increase the bunching and hence the gain.

Table 4.4: Second Design Parameters

Operation Voltage, V_0	15 kV
Beam Current, I_0	0.10 A
Pitch factor $\alpha = v_\perp/v_\parallel$	1.5
Design Mode	TE_{02}
Input Power, P_{in}	35 mW
Magnetic Field, B_0	5.11 T
Output Power	51 W
Bandwidth	918 MHz
Saturated Gain	32 dB

	Length(λ_0)	Radius(mm)	$f_0(GHz)$	Q_{ohm}	Q_{diff}
cav1	5.5	2.3995	140.	850	800
dft1	9.9	1.85			
cav2	5.5	2.410	139.8	690	
dft2	9.8	1.85			
cav3	5.5	2.410	139.8	690	
dft3	9.2	1.85			
cav4	5.5	2.410	139.8	690	
dft4	11.1	1.85			
cav5	5.5	2.4015	139.9	1300	660
upt	16.3				
dft5	12.6	4.0			
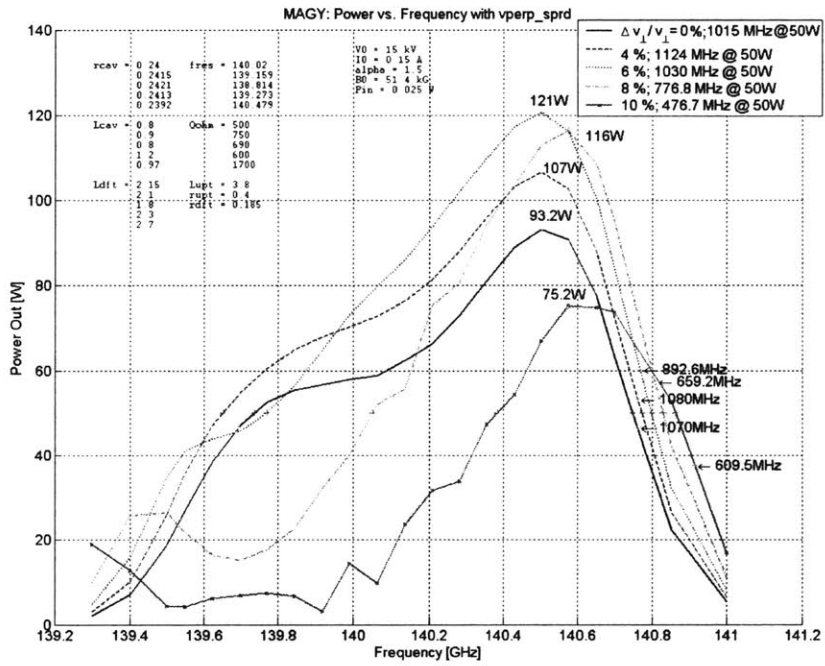
Figure 4-6: The effect of velocity spread on an amplifier system. The power increases up to a point and the peak shifts to higher frequencies due to the slower electrons. Note that the bandwidth at the 50-watt level around 140.8 GHz is increasing with increasing velocity spread.

There is a frequency shift evident as well in the figure as the peak shifts toward higher frequencies at higher velocity spread values, while the lower frequencies suffer a loss of gain (not an oversaturation). The tendency in this case is, to some extent, to shift the gain upward. Above approximately 6% in this case, the velocity spread begins to have only detrimental consequences.

4.4   Final Gyroklystron Design

In the final design, the beam current was increased to $I_0 = 150$ mA to increase the overall gain. With the larger gain allowance, a stronger stagger tuning was used to widen the bandwidth. It became apparent that the ability to vary the shape of the magnetic field profile could have helped widen bandwidth and increase efficiency, but nonetheless, quite a lot could be done with the flat profile we have. Having an adjustable profile means having an extra coil (gradient, trim or otherwise), extra leads, power supply and higher helium loss rate, adding approximately 30% to the cost of the magnet.

The larger amount of stagger tuning is apparent in the table for the final design, as the two extremes of the tuning vary by over 1%. Finding suitable tuning frequencies consisted of finding some feature at some frequency that should be changed, finding the cavity that is the likely cause and then tuning in accordingly. For example, cavities 4 and 5 are known to be very persuasive in their contributions to high power and bandwidth. If they are too close, oversaturation will result; too far and the power may fall.

The first cavity is very sensitive in terms of tuning. It should be tuned to within 1 micron (50 MHz), but even electroforming a cavity can only produce accuracy of 0.2 mils (300 MHz), so tuning by hammer or screw or some other means becomes important. Other cavities may only need to be tuned to within 100 MHz or more.

4.4.1   Final Design characteristics

To characterize this design, many parameters were varied over a reasonable range.

78

Table 4.5: Final Design Parameters

Operation Voltage, V_0	15 kV
Beam Current, I_0	0.15 A
Pitch factor $\alpha = v_\perp/v_\parallel$	1.5
Design Mode	TE_{02}
Input Power, P_{in}	25 mW
Magnetic Field, B_0	5.14 T

Output Power	129 W
Efficiency	5.7%
Bandwidth	1050 MHz
Bandwidth at 50W	1270 MHz
Saturated Gain	35 dB

	Length(λ_0)	Radius(mm)	$f_0(GHz)$	Q_{ohm}	Q_{diff}
cav1	3.73	2.400	140.02	500	800
dft1	16.1	1.85			
cav2	4.20	2.417	139.04	750	
dft2	9.33	1.85			
cav3	3.73	2.423	138.70	700	
dft3	11.2	1.85			
cav4	5.37	2.413	139.27	400	
dft4	14.5	1.85			
cav5	4.53	2.394	140.37	1700	360
upt	17.7				
dft5	12.6	4.0			
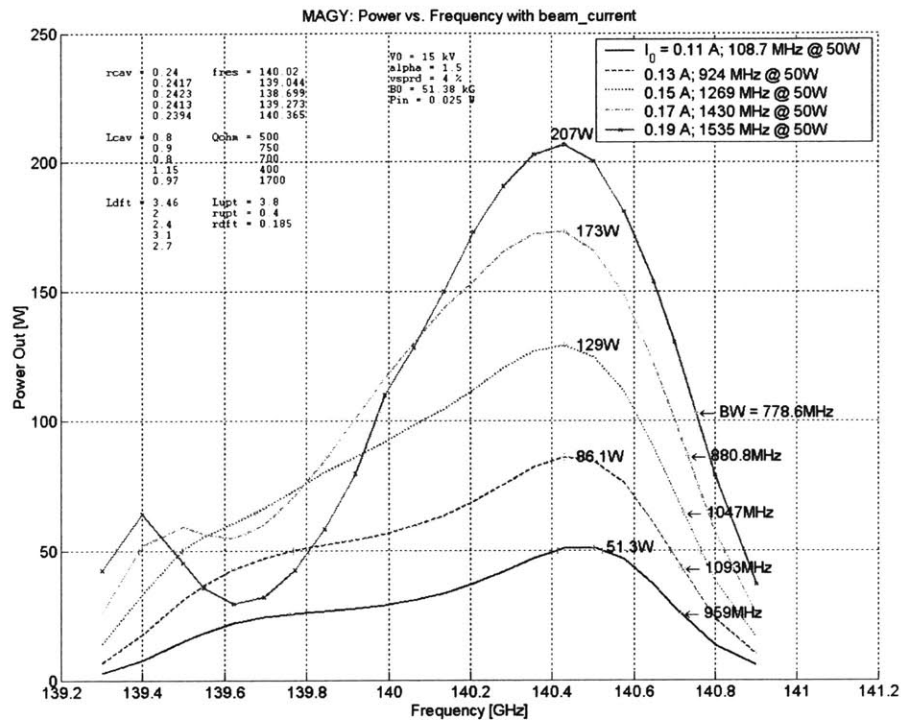
Figure 4-7: Current variations on the final design. The design value of current is I_0=0.15 A, showing a -3 dB bandwidth of 1050 MHz, a bandwidth of 1270 MHz at the 50 Watt level, and a peak power of 130 W.

Figure 4-7 shows variations of the beam current and their effect on the frequency spectrum of this design. At higher beam current, there seems to be an excess of gain around 139.7 GHz. If the GKL is operated at this beam current level, detuning the magnetic field may help relieve the oversaturation at that frequency.

In Figure 4-8, the effect of varying the magnetic field is seen. Over the B-field range of at least 51.3 kG to 51.5 kG, there is over 1 GHz of bandwidth available at the 50-Watt level. This 0.4% difference seems tolerable and the field drift specification for the magnet is <0.05 ppm/hour, meaning the magnet will have to be re-adjusted slightly every 10 years to maintain the proper operating regime.

Variations of the input power illustrate that the -3 dB bandwidth is typically lower at higher input powers, but the bandwidth at the 50-Watt level typically increases (Fig. 4-9). Again, some oversaturation is apparent around 139.7 GHz, as the output
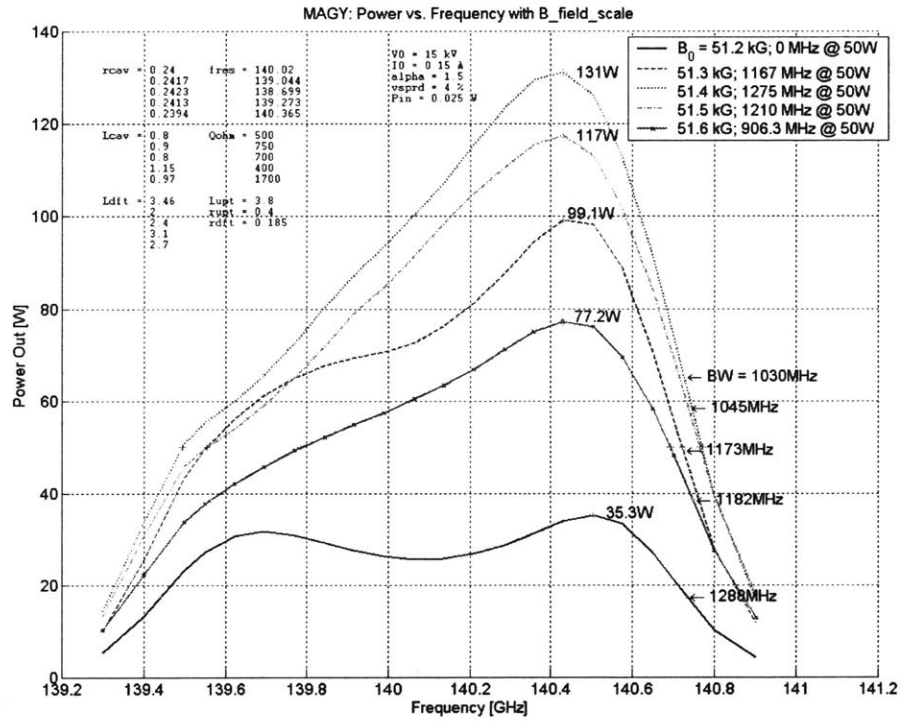
Figure 4-8: Magnetic field variations on the final design. The design value is $B_0 = 51.38$ kG. Even over a B_0 deviation of 0.4%, over 1 GHz of BW is available at 50 W.

MAGY: Power vs. Frequency with power_inp_perp_te(1)
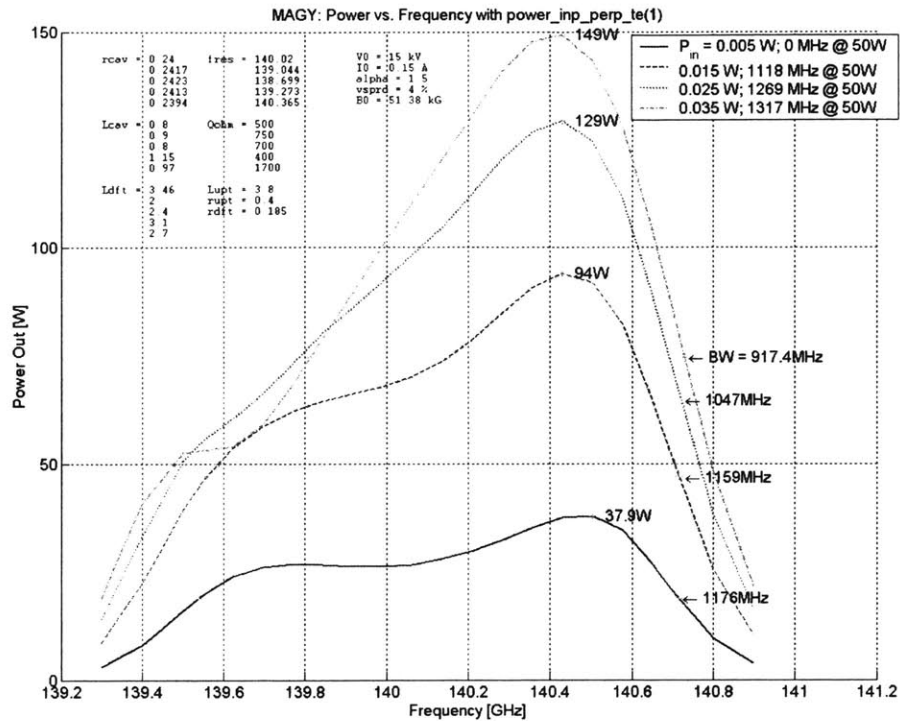
Figure 4-9: Input power variations: The design value is $P_{in}=25$ mW.

power decreases with increasing input power.

The gain of the device shows good behavior across a range of input powers (Fig. 4-10). The linear gain is around 39 dB and the saturated gain is 36 dB. The maximum saturated output power under these operating conditions is above 160 watts.

Figure 4-11 shows the effect of velocity spread. This design delivers over 1 GHz of bandwidth at the 50-watt level even at perpendicular spreads of 6% (13.5% parallel spread). Again, the peak in the power spectrum tends to shift to higher frequencies. This effect could be attributed to the output cavity, which is tuned to the highest frequency of 140.4 GHz and correspondingly peaks in magnetic field. The bandwidth and power tend to increase from 0% to 4% spread due to the cavities being tuned to a range of frequencies and therefore more easily excited by the spread in cyclotron frequencies.

The pitch factor (α) spread, shown in Fig. 4-12, reveals a high sensitivity on the performance of the amplifier to the value of α. This points to a preference for a triode
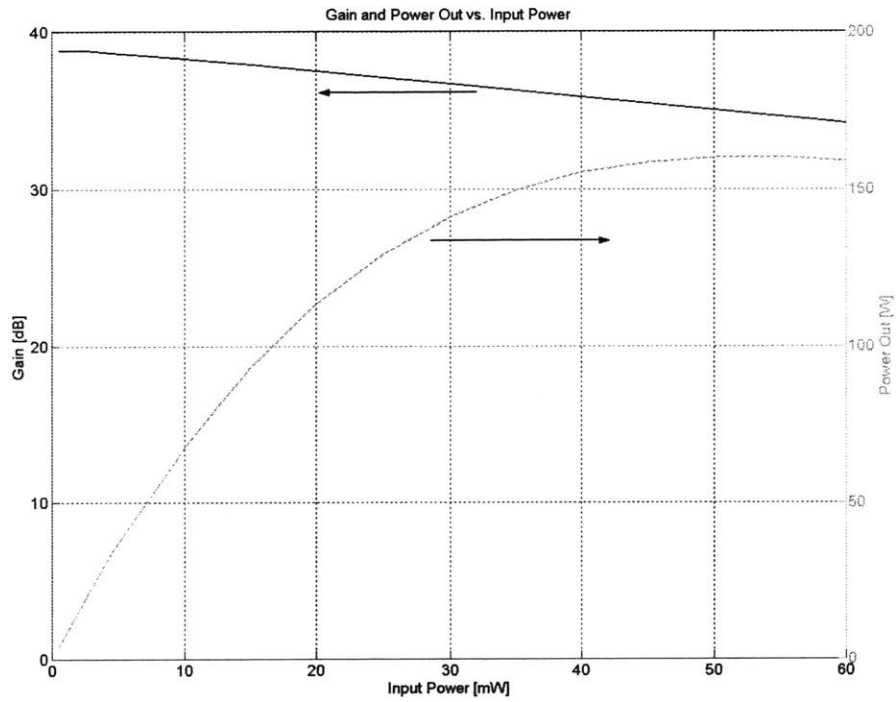
Figure 4-10: Gain and output power versus input power. The linear gain is 39 dB and the saturated gain is 36 dB. The frequency here was 140.5 GHz, roughly the peak of the power spectrum.

MAGY: Power vs. Frequency with vperp_sprd

Power Out [W]

Frequency [GHz]

rcav = 0.24   freq = 140.02   V0 = 15 kV
       0.2417   139.044   I0 = 0.15 A
       0.2423   138.699   alpha = 1.5
       0.2413   139.273   B0 = 51 38 kG
       0.2394   140.365   Pin = 0.025 W

lcav = 0.8   Qohm = 500
       0.4   750
       0.8   700
       1.15   400
       0.97   1700

ldft = 3.46   lup = 3.8
       2   rup = 0.4
       2.4   rdft = 0.185
       3.1
       2.7

△v⊥/v⊥ = 0 %; 1235 MHz @ 50W
4 %; 1269 MHz @ 50W
6 %; 1029 MHz @ 50W
8 %; 763.8 MHz @ 50W
10 %; 397.4 MHz @ 50W

131W
129W
123W
104W
65.3W

BW = 1113MHz →   ← 1047MHz ← 863.1MHz
                  ← 741.9MHz
                  ← 660.6MHz

Figure 4-11: Velocity spread variations. The design value was 4%, but it delivers over 1 GHz of BW at 50 W even with 6% spread.

Figure data (MAGY: Power vs. Frequency with pitch_ang):

Legend:
- α = 1.35; 258.6 MHz @ 50W
- 1.4; 634.7 MHz @ 50W
- 1.45; 1128 MHz @ 50W
- 1.5; 1269 MHz @ 50W
- 1.55; 1102 MHz @ 50W

rcav = 0.24   fres = 140.02
       0.2417   139.044
       0.2423   138.699
       0.2413   139.273
       0.2394   140.365

Lcav = 0.8   Qohm = 500
       0.9   750
       0.8   700
       1.15   400
       0.97   1700

Ldft = 3.46   Lupt = 3.8
       2   rupt = 0.4
       2.4   rdft = 0.185
       3.1
       2.7

V0 = 15 kV
I0 = 0.15 A
vsprd = 4 %
B0 = 51.38 kG
Pin = 0.025 W

Axis: Power Out [W] vs Frequency [GHz] (139.2 to 141.2)

Curve peak labels: 151W, 129W, 103W, 77.2W, 57.2W

Right-side annotations:
← BW = 866MHz
← 1047MHz
← 1111MHz
← 1074MHz
← 941MHz

Figure 4-12: Beam pitch factor (α) variations. The nominal value is 1.5 for the design.

electron gun to tune α to the required value. If this pitch factor is off, it can also be compensated for by adjusting the beam current.

The electric field profile in the cavities shows gain in each cavity at each frequency (Fig. 4-13). There is a visible electric field leakage between the last and penultimate cavities as a result of the finite copper conductivities, although it is not clear if this leakage has a significant influence on the simulation the device.
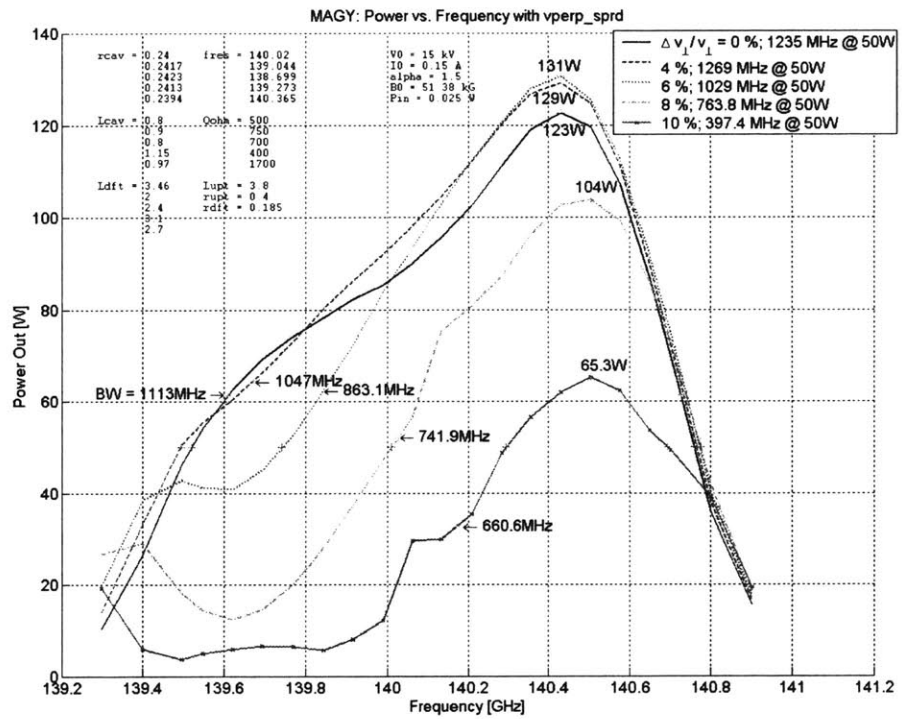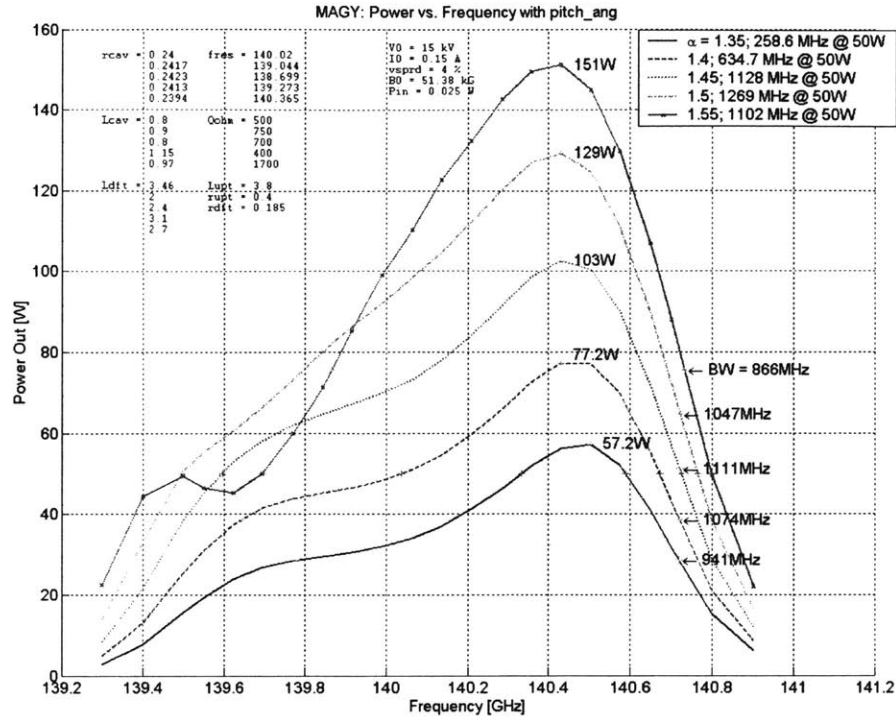
Figure 4-14 shows the short pulse behavior for a 4-ns trapezoidal input pulse at various frequencies. The propagation delay though the cavity circuit is around 1-ns. The pulses can be shortened to 1 or 2 ns with a slight reduction in output power. This delay is due to the propagation of the electron beam through the tube at about 13% the speed of light and will increase upon addition of the non-linear uptaper and mode converter. The peaks on, for example, the rising and falling edges of the 139.6 GHz pulse can be attributed to the fact that the gain increases at lower power levels.
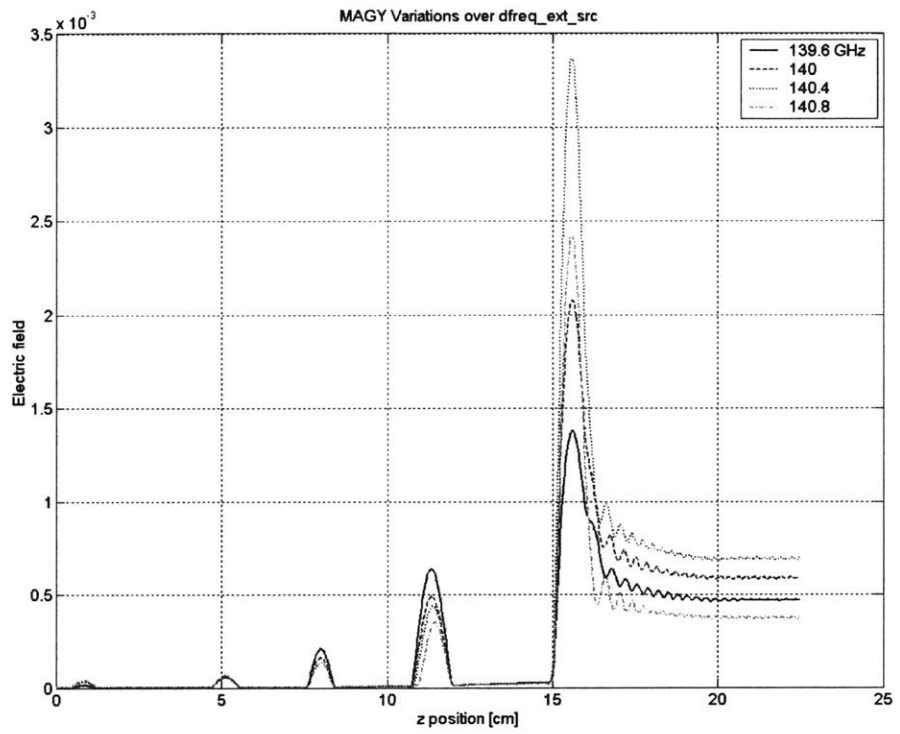
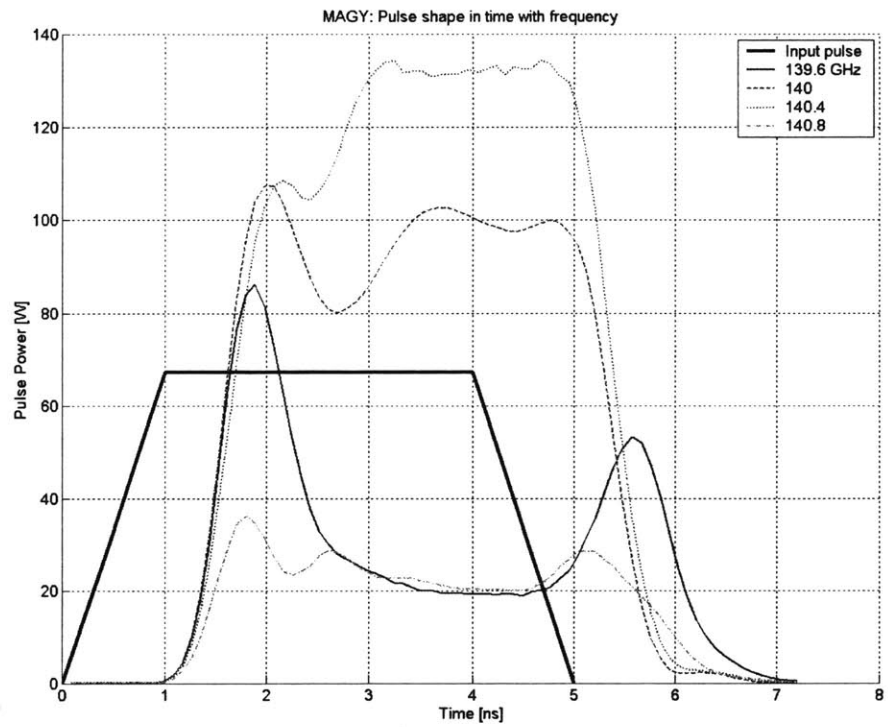Figure 4-13: The electric field profiles in the cavities for several frequencies.

Figure 4-14: The pulse shapes for a 4 ns trapezoidal pulse showing a propagation delay of approximately 1 ns.

4.5 Preliminary Input Coupler

Preliminary work was performed to construct a suitable input coupler to get the low power RF signal into the first cavity. HFSS was used to design a wrap-around coupler using the TE_{81} mode of a coaxial cavity with four coupling slots into the first cavity (Fig. 7-1). In this simple treatment, industry standard WR6 (0.065 x 0.0325 inch) rectangular waveguide was used for the input and ring resonator sections, as well as the four short segments that connect the ring to the cavity. The difficulty in designing this coupler is forming a clean TE_{02} mode inside the cavity over the frequency range of interest. The figure shows the HFSS simulations over 1 GHz with a decent TE_{02} mode shape in the cavity. Measurements on bandwidth and coupling were not made at this time.

4.6 Conclusions

In this section, the design of the gyroklystron cavity circuit was discussed in detail, with a focus on the optimization of the bandwidth and power. Three designs were presented highlighting the major milestones in the optimization of the gyroklystron. The final design was presented and variations on its characteristics were explored.

This theoretical final design seems solid, with some room for error in the maximum power and bandwidth. If some parameters fall short of their design values, such as the pitch factor, they can be compensated to some degree by external controls, such as beam current and magnetic field.

Preliminary work on a wrap-around input coupler was presented. This coupler uses the TE_{81} coaxial mode to couple to the TE_{02} mode in the input cavity using four slot couplers. The TE_{02} mode is reasonably well formed over the range 139.4 GHz to 140.3 GHz.
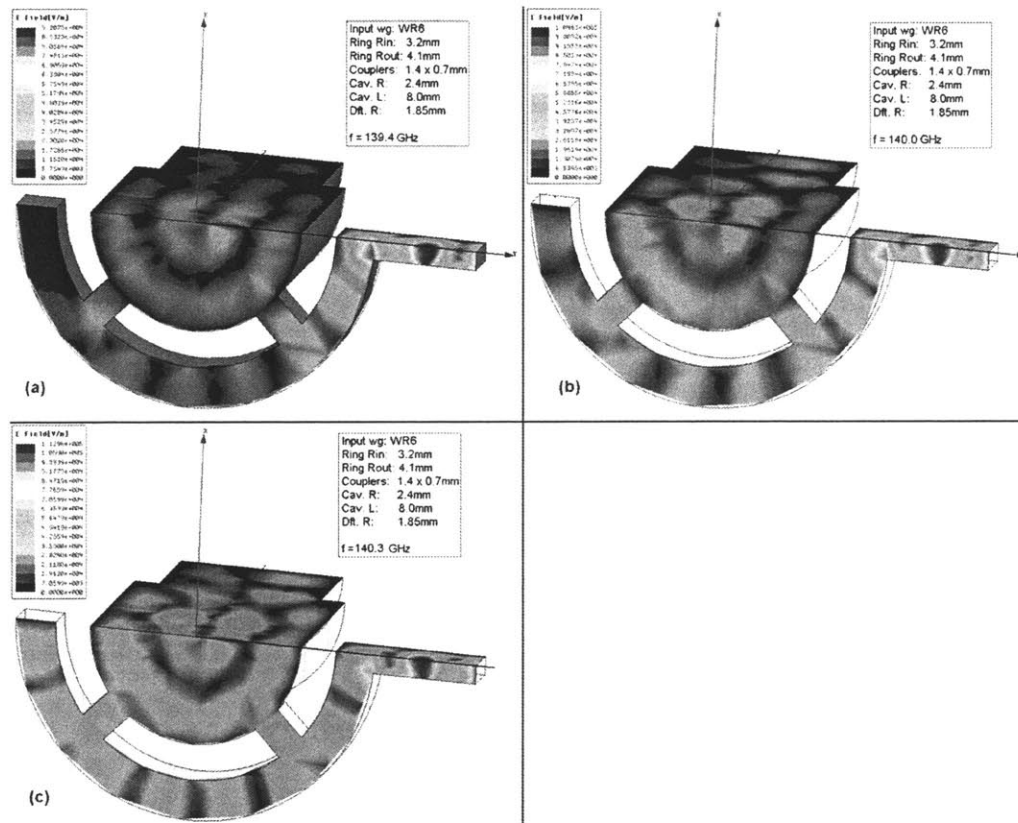
Figure 4-15: The preliminary work on the input coupler (quarter-slice shown): (a) 139.4 GHz; (b) 140.0 GHz; (c) 140.3 GHz.

Chapter 5

The Electron Gun

The performance of the electron gun design is essential to building a successful gyroklystron. The velocity spread must be as low as possible since the cavity circuit is rather long. Many non-ideal effects exist, including velocity spread due to cathode surface roughness and thermal non-uniformity, gun misalignment, insufficient vacuum, cathode poisoning, etc. All of these performance-hindering effects must be minimized for a successful result.

5.1   Overview

The electron gun consists of several major parts (Fig. 5-1). The filament heats the cathode uniformly to a suitably high temperature such that electrons are emitted by thermionic emission. The two anodes ("triode" MIG) and the cathode form a region where the equipotential contours are designed to guide the electrons along a proper path as they gain weakly relativistic energy. If the potentials are not carefully formed, the electron paths may cross (non-laminar flow) or sharp regions of the cathode (typically the "nose") may experience such high electric fields that breakdown occurs. The purpose of the second anode (a.k.a. the "mod-anode") is to adjust the potentials as an aid in obtaining the correct pitch factor ($\alpha = v_\perp / v_\parallel$). If, during the MIG design, the two anode potentials are identical, then only a single anode is required (diode MIG), simplifying the design and saving cost. Another reason to use a diode
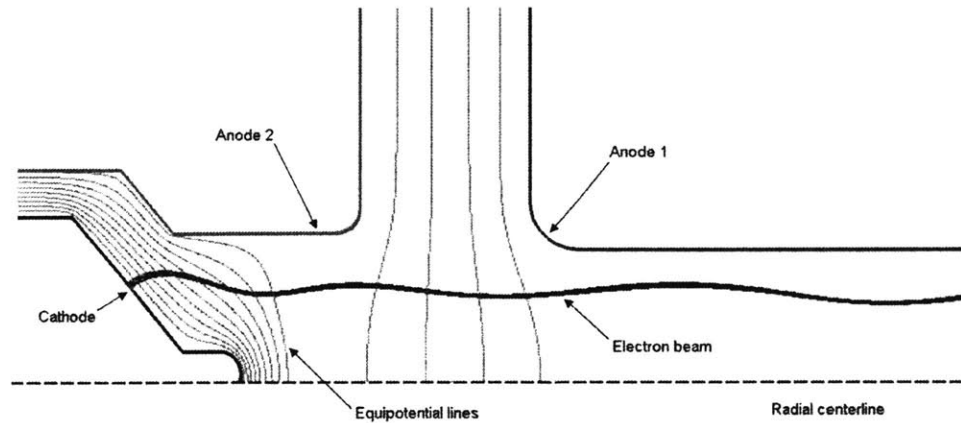
Figure 5-1: The MIG parts: Cathode, Anode 1, Anode 2 ("mod-anode"), shown with an electron beam and the equipotential contours.

instead of a triode is that it is not always easy to obtain an arbitrary voltage for the second anode, since lossy resistor dividers are commonly used. The diode power supply is thus simpler. Once the electrons are emitted, they are caught in a spiral around the magnetic fields lines as they are guided through the cavity circuit down to the collector region.

5.2 A 20 kV MIG design

Initial work early in the design focused on the electron gun since some information was needed to specify the magnet that would be required. During this time, extensive use of EGUN was made and design efforts pushed for both diode and triode designs. The beam voltage was chosen to be 20 kV, a value that later became 15 kV for the cavity circuit design. The design we present here is at 20 kV, but it could be scaled back to 15 kV with proper design modifications and still meet the requirements for the system. The triode design is presented because the diode gun had some difficulty keeping the space charge to acceptable limits. The triode gun will require some extra parts, but will also allow the beam α to be controlled to some extent.

The main goal of any MIG design is low velocity spread. These days, the transverse velocity spread due to beam optics is typically the lowest contributor to the total

Table 5.1: MIG Design Parameters

Parameter	Value	Unit
V_0	20	kV
I_0	0.1	A
Pitch factor, α	1.5	
Beam Radius, R_b	0.64	mm
Magnetic field at cavities	5.2	T
Cathode Radius	4.02	mm
Slant-length	0.5	mm
Current density	2	A/cm^2
Cathode slope	50	degrees
Cathode-Anode spacing factor	3	
Cathode temperature	1000	$^\circ C$
Cathode roughness	64×10^{-6}	inches
Cathode position*	55	cm
Results:		
α	1.59	
α spread	1.9	%
$\Delta v_\perp / v_\perp$ optical	0.55	%
$\Delta v_\perp / v_\perp$ thermal	1.3	%
$\Delta v_\perp / v_\perp$ roughness	4.0	%
Total velocity spread	4.2	%

(z=0 is center of magnetic field)*

spread and is around a few percent. The two other major contributions come from cathode roughness and thermal non-uniformity, which all together typically push the total transverse spread up to about 5%. Tab. 5.1 shows the design parameters and the results of this MIG design. The optical velocity spread is very low as well as the thermal spread estimate, but the estimate of velocity spread due to cathode surface roughness is very high (approx. 4%). By using a surface finish of 32 micro-inches instead of 64, this figure drops to about 2.8%. If this finer finish is realistic for a cathode this small (4.02 mm radius), the total spread could be as low as around 3%. This is rather difficult to achieve in practice, and even with the finer finish, we could expect the total spread to be elevated by 1 to 2% in practice.

The simulation result of 0.55% transverse velocity spread due to optics is a very good result. Rarely do gun designs achieve under 1% spread even in simulation. The
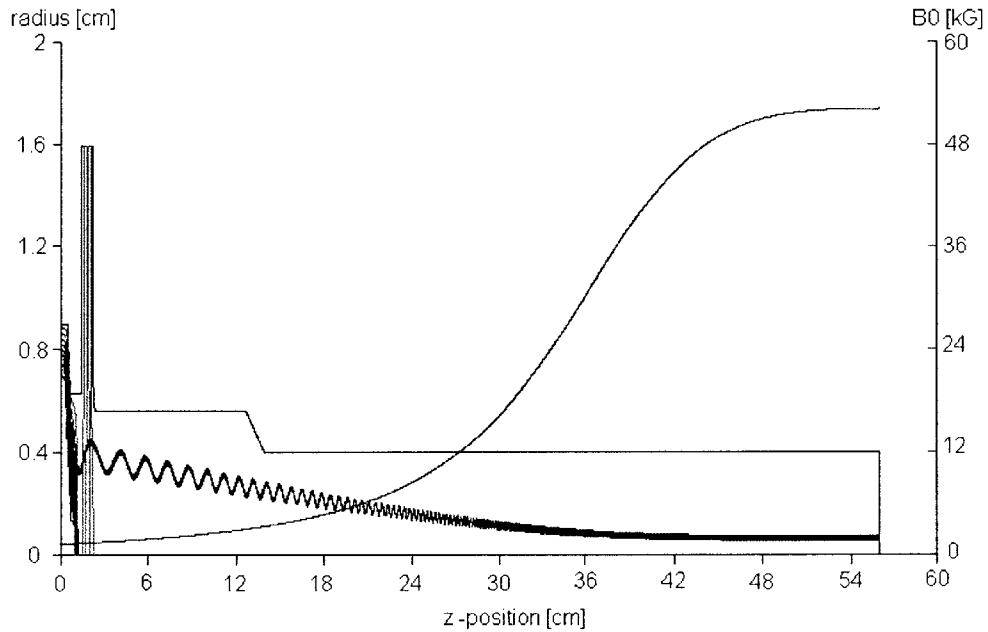
Figure 5-2: The EGUN simulation results for the 20 kV MIG design (Courtesy of J. R. Sirigiri).

reason for this low spread can be attributed to the fact that the beam current is rather low. Low beam current with a modest beam current density means that the emitter surface area can be quite small. Since the magnetic compression is rather high at 40, the cathode radius is fairly large, so the emitter slant length is very short. Also, there is even less of a difference in electron trajectory lengths because the cathode angle is quite high.

The predicted α value of 1.59 is slightly over the design value of 1.5, but to compensate, the beam current could be lowered slightly, or the mod-anode voltage could be altered (causing the velocity spread to rise slightly). The alpha spread of under 2% is also phenomenal.

Fig. 5-2 shows the EGUN output for the simulation run from the cathode to the center of the magnetic field. A blow-up of the electron beam, equipotential contours, and cavity shape is shown back in Fig. 5-1.

Fig. 5-3 shows the dimensions of the gun section used for the EGUN simulation. The cathode is at -20 kV, the mod-anode is at -14.7 kV and the main anode is at
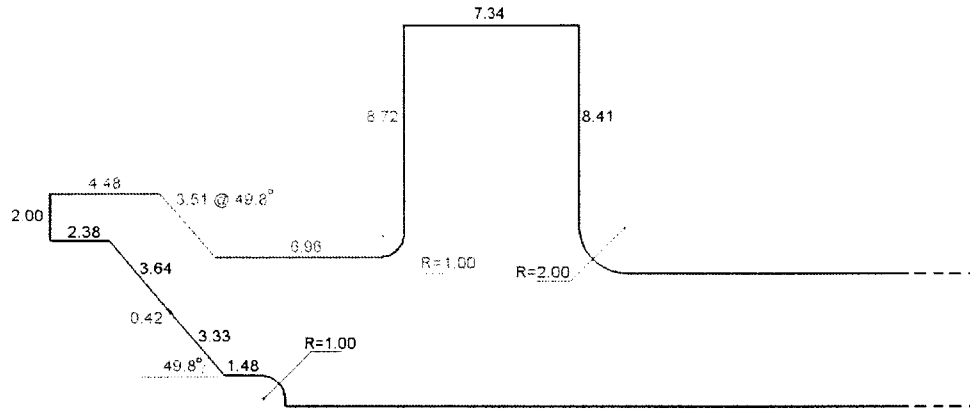
Figure 5-3: The dimensions in millimeters of the gun section used for the EGUN simulation.

ground potential (0 V).

5.3 Conclusion

In this chapter, a 20 kV MIG design was presented with a remarkably low perpendicular optical spread of only 0.55%. Such low spreads will be necessary for the operation of a successful electron gun. The velocity spread due to roughness is by far the limiting factor to keeping the total velocity spread low, so steps must be taken to ensure a smooth finish on the emitter surface. Although the design was for a 20 kV beam as presented, similar results should be achievable at the lower beam voltage of 15 kV with proper design modifications.

Chapter 6

The Output Section

In this chapter, the designs of the gyroklystron output section and mode converter are discussed. A nonlinear uptaper was designed to replace a portion of the linear uptaper in the gyroklystron design in order to minimize mode conversion. Following the output section is the mode converter region, which converts the TE_{02} mode coming out from the gyroklystron circuit to the TE_{01} mode. The electron beam is collected in a region just past the mode converter.

6.1   Nonlinear Uptaper

The output section of the gyroklystron consists of the final cavity, a linear uptaper and a nonlinear uptaper. A diagram of this output section is shown in Fig. 6-1. The nonlinear uptaper consists simply of a fillet that suppresses mode conversion. CASCADE [48] was used to estimate the mode purity to be 99.98% at the center frequency of 140 GHz.

6.2   Mode Converter

The equations from Chap. 3 were used to get an idea of the expected bandwidth and size of the mode converter. The resulting mode converter design was evaluated in CASCADE [48] and the results of the simple theory and CASCADE simulations are
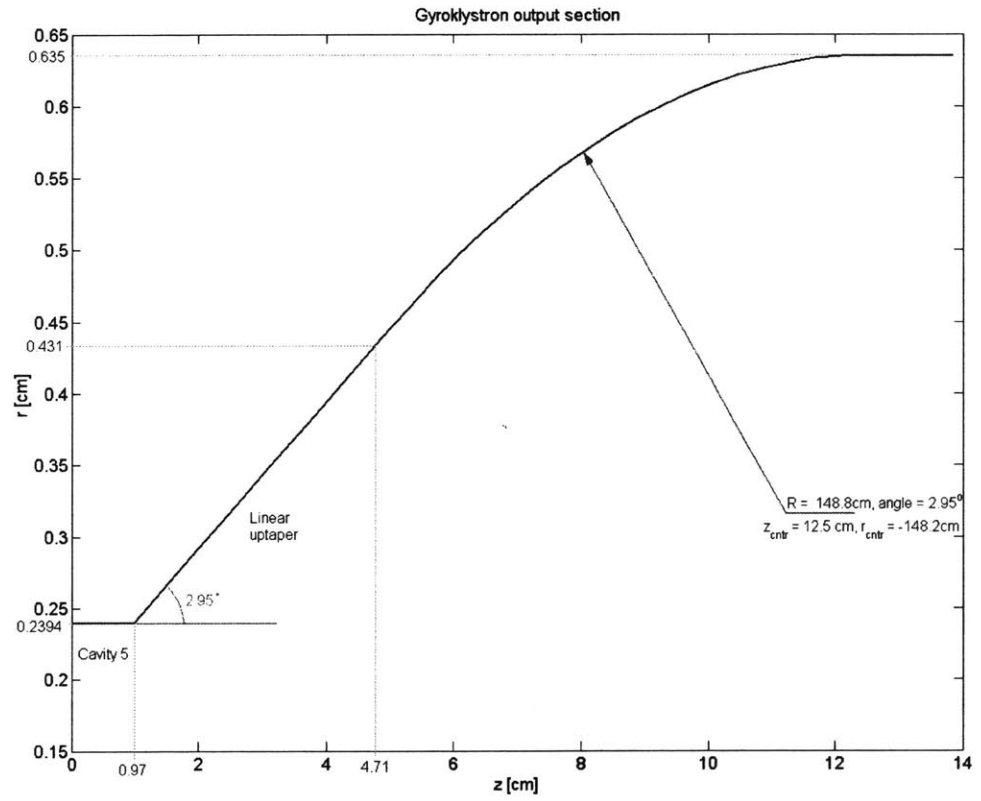
Figure 6-1: The gyroklystron output section consisting of linear and nonlinear uptaper sections.
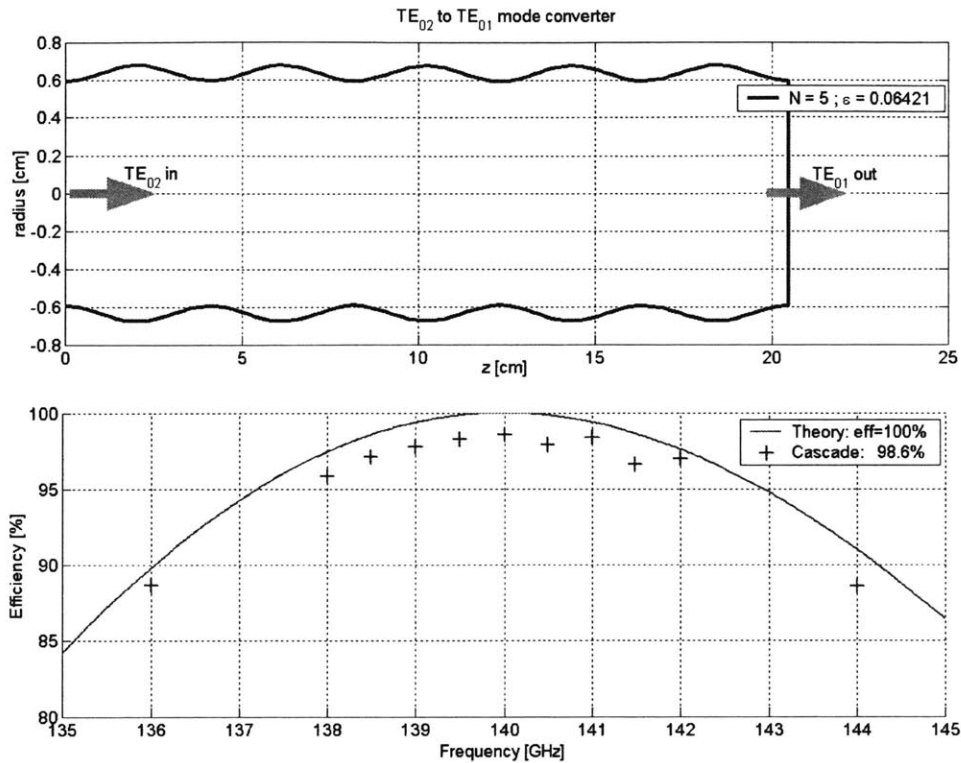
Figure 6-2: The results of the simple equations and the CASCADE simulations show reasonable agreement. The mode converter consists of $N = 5$ periods and has a bandwidth of 14 GHz and a peak efficiency of 98.6%.

shown in Fig. 6-2. Using $N = 5$ periods gives good bandwidth and efficiency, as well as a relatively short mode converter. Over the frequency range of interest (139 GHz to 141 GHz), the conversion is typically better than 98%.

6.3   Complete Output Section

The nonlinear uptaper and mode converter were put together in CASCADE for evaluation. Mode purity from the final cavity all the way to the end of the mode converter remained above 98% over the frequency range from 140 to 141 GHz (frequencies below 140 GHz are cut off in the final cavity and cannot be evaluated without an electron beam).

6.4   Conclusion

In this section, the nonlinear uptaper and mode converters were presented. The nonlinear uptaper yielded greater than 99% mode purity over the frequency range of interest. When the nonlinear uptaper and mode converter were joined together, the TE_{02} mode was converted to TE_{01} with over 98% efficiency in theory over the band of interest. These results seem reasonable and meet the goals of the design.

Chapter 7

Discussion and Conclusions

The tradeoffs, theory and design of a 140 GHz, 100 W gyroklystron amplifier have been presented in this thesis. The gyroklystron consists of a series of cavities each tuned to a specific frequency. The benefits of this method are high gain and wide bandwidth from a low voltage device as well as good linearity and very low noise. This work is specifically designed to meet our needs and is an extension to the previous foundational work done by others. This design included detailed studies on the electron gun, cavity circuit, and mode converter, as well as the background and theory for each. Several established simulation codes were used in the design of this vacuum electron device.

The overall goals of this experiment were 1 GHz of -3 dB bandwidth with a peak of 100 W with the capability to run from nanosecond-scale short pulses to full continuous wave operation. This design achieved a 130 Watt output at over 1 GHz of -3 dB bandwidth and a bandwidth of nearly 1.3 GHz at the 50-Watt level. The design also performs well with nanosecond-scale short pulses over the whole frequency range. While some parameters in the design, such as the pitch factor, α, are somewhat sensitive, they can be compensated for by external controls, like beam current and magnetic field. The circuit can provide over 1 GHz of bandwidth at the 50-Watt level over a magnetic field deviation of 0.4%, meaning the superconducting magnet will need to be re-tuned approximately once every ten years. The circuit design theoretically meets the specifications over the range of approximately 4% to

6% transverse velocity spread (9% to 13.5% parallel spread), a robustness that other designs may not deliver.

7.1 Future Work

Following the acceptance of this thesis, the evaluation of other possible designs such as the gyro-TWT or gyrotwystron will begin if necessary. While the gyroklystron promises to meet the specifications in theory, the actual construction and demonstration of such a five-cavity device is rather difficult, as very careful tuning is required to obtain the correct cavity characteristics. A gyro-TWT is perhaps easier to build, as it is most simply a straight copper pipe with distributed loss added, but it may be difficult to troubleshoot, as backward waves and spurious modes are difficult to suppress correctly. Furthermore, reliable sources for the necessary precision lossy ceramic parts are scarce and slow to deliver, and many of the other materials have not been fully or properly characterized. A gyrotwystron, on the other hand, while having the benefits of both of the aforementioned methods, also suffers from the disadvantages of both. Newer possibilities, such as the Confocal-TWT or PBG-based solutions, may be too risky to pursue at this time, simply because those designs have not been widely explored experimentally. In light of these remarks, perhaps the gyroklystron would be most suitable after all.

7.2 A 500 W Gyroklystron

There has been interest in a 140 GHz, 500 W gyroklystron with perhaps 2 GHz of bandwidth. This device could be more useful to the FBML as they attempt to perform DNP Electron Paramagnetic Resonance (EPR) measurements using a train of pulses approximately 1 nanosecond in duration. In order to get enough energy to their probe in such a short time, an estimate of 500 W is needed. Designing such a device in theory is a reasonable extension to the 100 W design. Currently, however, RF switch technology has not been able to provide switches with turn-on and turn-off times
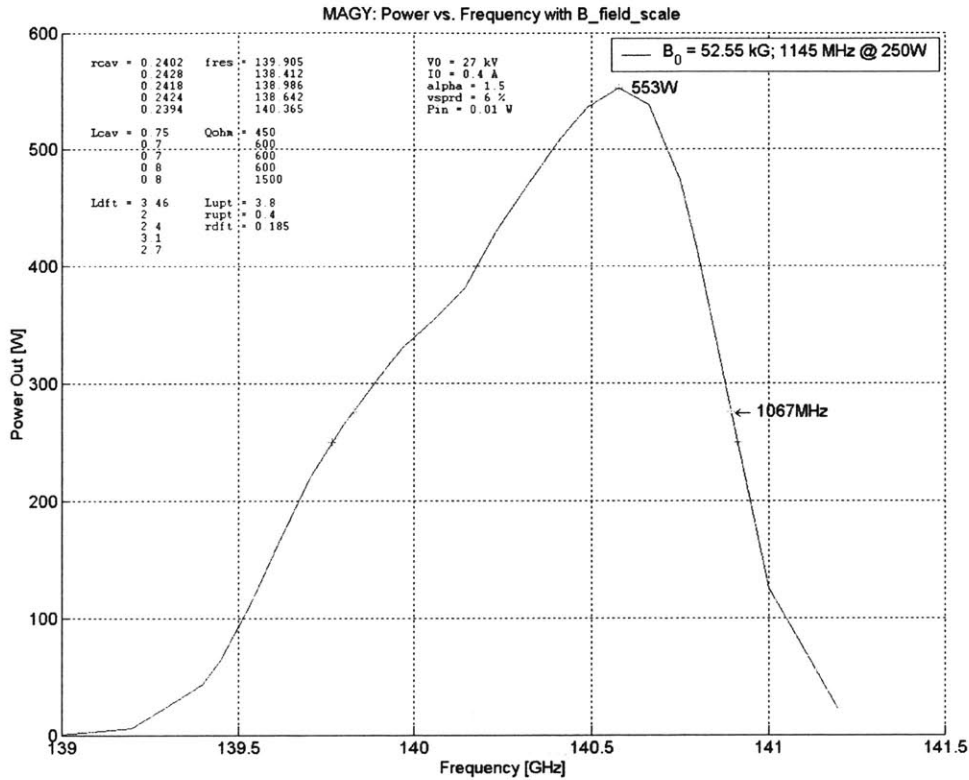
MAGY: Power vs. Frequency with B_field_scale

Power Out [W]

600

500

400

300

200

100

0

139   139.5   140   140.5   141   141.5

Frequency [GHz]

rcav = 0.2402
       0.2428
       0.2418
       0.2424
       0.2394

fres = 139.905
       138.412
       138.986
       138.642
       140.365

V0 = 27 kV
I0 = 0.4 A
alpha = 1.5
vsprd = 6 %
Pin = 0.01 W

Lcav = 0.75
       0.7
       0.7
       0.8
       0.8

Qohm = 450
       600
       600
       600
       1500

Ldft = 3.46
       2
       2.4
       3.1
       2.7

Lupt = 3.8
rupt = 0.4
rdft = 0.185

B_0 = 52.55 kG; 1145 MHz @ 250W

553W

← 1067MHz

Figure 7-1: The preliminary design of a 500 W gyroklystron circuit with a 27 kV, 0.4 A electron beam and saturated gain of 47.4 dB at 6% transverse velocity spread.

below 1 ns that meet our power level requirements. Nonetheless, some preliminary work is presented here in reaching toward a 500 W, 140 GHz gyroklystron with 2 GHz of -3 dB bandwidth.

The first requirement to reaching higher power is to increase the beam power. Using a 27 kV, 0.4 A electron beam and re-tuning the cavity circuit, it was possible to achieve an output of over 550 W with a bandwidth of over 1 GHz (over 1.1 GHz at the 250 W level). The input power was reduced to 10 mW and a transverse velocity spread of 6% was selected, resulting in a saturated gain of 47.4 dB. Other parameters for this preliminary design are given in Tab. 7.1. No careful optimizations were made for this design, and it is possible that the desired results could be achieved with only four cavities instead of five, which is an attractive possibility.

Table 7.1: 500 W GKL Preliminary Design Parameters

Operation Voltage, V_0	27 kV
Beam Current, I_0	0.4 A
Pitch factor $\alpha = v_\perp/v_\parallel$	1.5
Design Mode	TE_{02}
Input Power, P_{in}	10 mW
Magnetic Field, B_0	5.26 T
Output Power	553 W
Efficiency	5.1%
Bandwidth	1067 MHz
Bandwidth at 250W	1145 MHz
Saturated Gain	47.4 dB

	Length(λ_0)	Radius(mm)	$f_0(GHz)$	Q_{ohm}	Q_{diff}
cav1	3.50	2.402	139.905	450	800
dft1	16.1	1.85			
cav2	3.27	2.428	138.412	600	
dft2	9.35	1.85			
cav3	3.27	2.418	138.986	600	
dft3	11.2	1.85			
cav4	3.74	2.424	138.642	600	
dft4	14.5	1.85			
cav5	3.74	2.394	140.37	1500	360
upt	17.8				
dft5	12.6	4.0			

Bibliography

[1] R. O. Twiss, "Radiation transfer and the possibility of negative absorption in radio astronomy," *Aust. J. Phys.*, vol. 11, pp. 567–579, 1958.

[2] V. L. Granatstein, B. Levush, B. G. Danly, and R. K. Parker, "A quarter century of gyrotron research and development," *IEEE Transactions on Plasma Science*, vol. 25, no. 6, pp. 1322–1335, 1997.

[3] B. G. Danly, M. Blank, J. P. Calame, S. Cooke, B. Levush, W. Manheimer, A. McCurdy, K. T. Nguyen, D. E. Pershing, J. Petillo, R. K. Parker, T. A. Hargreaves, A. Theiss, R. B. True, K. L. Felch, T. S. Chu, H. Jory, P. Borchard, W. G. Lawson, and T. M. Antonsen, "Development of a W-band gyroklystron for radar applications," *22nd Int. Conf Infrared and Millimeter Waves, VA*, 1997.

[4] A. V. Gaponov-Grekhov and V. L. Granatstein, *Applications of high-power microwaves*. Boston: Artech House, 1994.

[5] K. L. Felch, B. G. Danly, H. R. Jory, K. E. Kreischer, W. Lawson, B. Levush, and R. J. Temkin, "Characteristics and applications of fast-wave gyrodevices," *Proc. IEEE*, vol. 87, pp. 752–781, 1999.

[6] L. R. Becerra, G. J. Gerfin, R. J. Temkin, D. J. Singel, and R. G. Griffin, "Dynamic nuclear polarization with a cyclotron resonance maser at 5 tesla," *Physical Review Letters*, vol. 71, no. 21, pp. 3561–3564, 1993.

[7] G. Bar, M. Bennati, T. Nguyen, J. Ge, J. Stubbe, and R. G. Griffin, "High frequency (140 GHz) time domain EPR and ENDOR spectroscopy: The tyrosyl

radical-diiron cofactor in ribonucleotide reductase from yeast," *Journal of the American Chemical Society*, vol. 123, no. 15, pp. 3569–3576, 2001.

[8] V. L. Granatstein, R. K. Parker, and C. M. Armstrong, "Vacuum electronics at the dawn of the twenty-first century," *Proceedings of the IEEE*, vol. 87, no. 5, pp. 702–716, 1999.

[9] T. Idehara, I. Ogawa, S. Mitsudo, M. Pereyaslavets, N. Nishida, and K. Yoshida, "Development of a frequency tunable, medium power gyrotron (gyrotron FU series) as submillimeter wave radiation sources," *IEEE Transactions on Plasma Science*, vol. 27, no. 2, pp. 340–354, 1999.

[10] A. Kesar and E. Jerby, "Phase and gain measurements in a distributed-loss cyclotron-resonance maser amplifier," *Physical Review E*, vol. 65, p. 036503ff, 2001.

[11] G. S. Nusinovich, B. Levush, and B. Danly, "Gain and bandwidth in stagger-tuned gyroklystrons and gyrotwystrons," *IEEE Transactions on Plasma Science*, vol. 27, no. 2, pp. 422–428, 1999.

[12] G. S. Nusinovich, T. M. Antonsen, Jr., H. Guo, and V. L. Granatstein, "Theory of clustered-cavity gyroklystrons," *Physics of Plasmas*, vol. 9, no. 9, pp. 4032–4039, 2002.

[13] V. L. Granatstein and I. Alexeff, *High power microwave sources*. Boston: Artech House, 1987. and references therein.

[14] M. V. Kartikeyan, E. Borie, and M. K. A. Thumm, *Gyrotrons*. New York: Springer, 2004.

[15] K. E. Kreischer, B. G. Danly, J. B. Schutkeker, and R. J. Temkin, "The design of megawatt gyrotrons," *IEEE Transactions on Plasma Science*, vol. PS-13, no. 6, pp. 364–373, 1985.

[16] J. Sirigiri, *A Novel Wideband Gyrotron Travelling Wave Amplifier*. PhD thesis, Massachusetts Institute of Technology, 2003.

[17] J. R. Sirigiri, K. E. Kreischer, J. Machuzak, I. Mastovsky, M. A. Shapiro, and R. J. Temkin, "Photonic-band-gap resonator gyrotron," *Physical Review Letters*, vol. 86, pp. 5628–5631, 2001.

[18] T. M. Tran, B. G. Danly, K. E. Kreischer, J. B. Schutkeker, and R. J. Temkin, "Optimization of gyroklystron efficiency," *Physics of Fluids*, vol. 29, no. 4, pp. 1274–1281, 1986.

[19] M. Blank, B. G. Danly, B. Levush, K. T. Nguyen, D. E. Pershing, K. Felch, B. G. James, P. Borchard, P. Cahalan, T. S. Chu, H. Jory, and J. P. Calame, "Experimental demonstration of W-band gyroklystron amplifiers with improved gain and efficiency," *IEEE Transactions on Plasma Science*, vol. 30, no. 3, pp. 865–875, 2002.

[20] M. Garven, J. P. Calame, K. T. Nguyen, B. Danly, B. Levush, and F. N. Wood, "Experimental studies of a four-cavity, 35 GHz gyroklystron amplifier," *IEEE Transactions on Plasma Science*, vol. 28, no. 3, pp. 672–680, 2000.

[21] M. Blank, B. G. Danly, and B. Levush, "Experimental demonstration of W-band gyroklystron amplifiers with improved gain and efficiency," *IEEE Transactions on Plasma Science*, vol. 28, no. 3, pp. 706–711, 2000.

[22] M. Blank, B. G. Danly, B. Levush, and D. E. Pershing, "Experimental investigation of W-band (93 GHZ) gyroklystron amplifiers," *IEEE Transactions on Plasma Science*, vol. 26, pp. 409–415, 1998.

[23] B. G. Danly, M. Blank, J. P. Calame, B. Levush, K. T. Nguyen, D. E. Pershing, R. K. Parker, K. L. Felch, B. G. James, P. Borchard, P. Calahan, T. S. Chu, H. R. Jory, T. A. Hargreaves, R. B. True, W. G. Lawson, and T. M. Antonsen, "Development and testing of a high-average power, 94-GHz gyroklystron," *IEEE Transactions on Plasma Science*, vol. 28, no. 3, pp. 713–726, 2000.

[24] G. S. Nusinovich, M. T. Walter, M. Kremer, M. E. Read, and D. Boehme, "Submillimeter-wave gyroklystron: theory and design," *IEEE Transactions on Plasma Science*, vol. 28, no. 3, pp. 936–944, 2000.

[25] X. Xu, W. Lawson, C. Liu, J. Cheng, B. Hogan, V. L. Granatstein, and M. Reiser, "Design of a new concept cavity for high power gyroklystrons," *IEEE International Conference on Plasma Science*, vol. 3P27, p. 198ff, 1998.

[26] J. D. McNally, D. B. McDermott, Q. S. Wang, F. V. Hartemann, and N. C. Luhmann, Jr., "High performance, 70 kV third-harmonic smooth-bore gyroklystron amplifier," *IEEE Transactions on Plasma Science*, vol. 22, no. 5, pp. 932–938, 1994.

[27] P. E. Latham, "AC space-charge effects in gyroklystron amplifiers," *IEEE Transactions on Plasma Science*, vol. 18, no. 3, pp. 273–285, 1990.

[28] E. V. Zasypkin, M. A. Moiseev, E. V. Sokolov, and V. K. Yulpatov, "Effect of penultimate cavity position and tuning on three-cavity gyroklystron amplifier performance," *International Journal of Electronics*, vol. 78, no. 2, pp. 423–433, 1995.

[29] G. S. Nusinovich, B. Levush, and B. Danly, "Theory of multi-beam stagger-tuned gyroklystrons," *IEEE Transactions on Plasma Science*, vol. 26, pp. 475–481, 1998.

[30] M. Hornstein, "Design of a 460 GHz second harmonic gyrotron oscillator for use in dynamic nuclear polarization," Master's thesis, Massachusetts Institute of Technology, 2001.

[31] A. Cavallo, J. Doane, and R. Cutler, "Low-loss broadband multimode corrugated waveguide performance," *Rev. Sci. Instrum., AIP*, vol. 61, no. 9, pp. 2396–2400, 1990.

[32] J. M. Baird and W. Lawson, "Magnetron injection gun (MIG) design for gyrotron applications," *International Journal of Electronics*, vol. 61, no. 6, pp. 953–967, 1986.

[33] S. E. Tsimring, "On the spread of velocities in helical electron beams," *Radiophysics of Quantum Electronics*, vol. 15, pp. 952–961, 1972.

[34] W. B. Hermannsfeldt, "EGUN - an electron optics and gun design program," Technical report SLAC-331, UC-28, Stanford Linear Accelerator Center, October 1988.

[35] Tricomp2D suite, TRACK v6.0. Version 5.0, Field Precision, Albuquerque, NM, 2002.

[36] AMaze3D suite, OMNITRACK. Version 5.0, Field Precision, Albuquerque, NM, 2003.

[37] MICHELLE electron gun and collector modeling tool. Various versions, SAIC, MD, 2000.

[38] V. A. Flyagin, A. L. Gol'denberg, and G. S. Nusinovich *Infrared and Millimeter Waves*, vol. 11, pp. 179–226, 1984.

[39] A. W. Fliflet, M. E. Read, K. R. Chu, and R. Seeley *International Journal of Electronics*, vol. 53, pp. 505–521, 1982.

[40] High Frequency Structure Simulator (HFSS). Version 9.1, Ansoft Corporation, Pittsburg, PA, 2003.

[41] M. Botton and T. M. Antonsen, Jr., "MAGY: A time-dependent code for simulation of slow and fast microwave sources," *IEEE Transactions on Plasma Science*, vol. 26, no. 3, pp. 882–892, 1998.

[42] B. Goplen, L. Ludeking, D. Smithe, and G. Warren, "User configurable MAGIC code for electromagnetic PIC calculations," *Comput. Phys. Commun.*, vol. 27, p. 54ff, 1995.

[43] J. P. Verboncoeur, A. B. Langdon, and N. T. Gladd, "An object oriented electromagnetic PIC code," *Comput. Phys. Commun.*, vol. 87, p. 199ff, 1995.

[44] T. Weiland, "Computing in accelerator design and operation," *Proc. Europhysics Conf., Lecture Notes in Physics. Berlin Germany*, vol. 215, p. 21ff, 1983.

[45] C. L. Chang, D. Chernin, A. Drobot, K. Ko, M. Kress, A. Mankovsky, A. Mondelli, and J. Petillo, "Three-dimensional modeling of accelerators," *Proc. Conf. Computer Codes and Linear Accelerator Community, LANL*, vol. LA-11875-C, p. 27ff, 1990.

[46] B. Z. Katsenelenbaum, L. Mercer del Rio, M. Pereyaslavets, M. Sorolla Ayza, and M. Thumm, *Theory of Nonuniform Waveguides*. London: Institution of Electrical Engineers, 1998. and references therein.

[47] M. Thumm, "High power mode conversion for linearly polarized HE11 hybrid mode output," *Int. J. Electron.*, vol. 61, pp. 1135–1153, 1986.

[48] Cascade. Cascade engine V1.60, Calabazas Creek Research, Inc., Saratoga, CA, 2001.

[49] B. Levush, M. Blank, J. Calame, B. Danly, K. Nguyen, D. Pershing, S. Cooke, P. Latham, J. Petillo, and T. Antonsen, Jr., "Modeling and design of millimeter wave gyroklystrons," *Physics of Plasmas*, vol. 6, no. 5, pp. 2233–2240, 1999.